DOSE AND RISK ASSESSMENT METHODS FOR EPIDEMIOLOGIC STUDIES

INVESTIGATING LONG-TERM SIDE EFFECTS OF PROTON THERAPY

A Dissertation

by

GLEB ANDREJEVICH KUZMIN

Submitted to the Office of Graduate and Professional Studies of
Texas A&M University
in partial fulfillment of the requirements for the degree of

DOCTOR OF PHILOSOPHY

Chair of Committee,	Gamal Akabani Hneide
Committee Members,	John Ford
	Michael Deveau
	Heather Wilson-Robles
	Joe Kornegay
	Choonsik Lee
Head of Department,	Yassin Hassan

August 2018

Major Subject: Nuclear Engineering

ABSTRACT

Proton therapy has been substantially growing in use and acceptance for the treatment of cancer in the past years. However, the long-term risks of secondary malignancies possibly associated with proton therapy have not been studied in detail due to the lack of well-established methodology and available patient information. Organ-specific radiation dosimetry in proton therapy is complicated but crucial in epidemiological investigations of radiotherapy patients. Scatter neutrons generated in the treatment head and inside the patient via nuclear interactions need to be taken into account in normal tissue dose assessment. The present study establishes the dosimetry methods for patient-specific organ dose calculations from proton therapy and methods to improve dose reconstruction of organ doses in out-of-field regions not typically covered by radiographic images.

First, using limited radiographic data from Computed Tomography (CT) modalities combined with the library of body size-dependent computational human phantoms, methods were created to generate a full-body patient-specific phantom. This allows for full-body neutron dose calculations using Monte Carlo radiation transport methods. Second, a computer simulation model was developed to reconstruct a patient-specific proton therapy treatment within Monte Carlo radiation transport codes using already available patient radiotherapy log files and reference measurements from the Maryland Proton Treatment Center (MPTC). The method will allow for calculation of normal tissue dose in patients at MPTC and will be extended to other proton therapy

machines installed at other proton therapy facilities. Finally, based on the normal tissue doses calculated for the pediatric phantoms, the risk of second neoplasms was calculated based on the BEIR VII risk models. Two pediatric computational phantoms were imported into the treatment planning system at MPTC.

Full-body organ dose calculations were carried out using the Monte Carlo calculation modules developed in the current study and the radiation weighting factors reported by the International Commission on Radiological Protection (ICRP) followed by the assessment of the risks of developing second neoplasms. Lifetime attributable risk were low, maximum being for the lungs of 0.111% for the one-year-old case and 0.108% for the five-year-old case.

In conclusion, key methods for normal tissue dosimetry in proton therapy patients were developed and validated. Methods established in this dissertation will be applied to support ongoing international epidemiologic studies of pediatric patients undergoing proton therapy.

ACKNOWLEDGEMENTS

CONTRIBUTORS AND FUNDING SOURCES

Contributors

Funding Sources

TABLE OF CONTENTS

LIST OF FIGURES

LIST OF TABLES

1   INTRODUCTION

1.1   BACKGROUND

In the last several decades, advances in cancer treatments and early detection have greatly increased the likelihood of post-treatment patient survival. Overall, the number of cancer survivors in the United States has tripled since 1971 and has been growing by 2% each year [1]. The likelihood that children with cancer will survive 5 years or longer after treatment has increased by more than 50% between 1975 and 2006 [2]. One reason for this increasing success has been due to advancements in radiation therapy, with nearly two-thirds of all cancer patients receiving radiotherapy as part of their treatment [3]. During treatment of patients with solid cancers, the main concern is to irradiate the cancerous tissue enough to damage. A treatment plan is optimized to maximize the tumor dose while minimizing the dose to normal tissue near the treatment site to avoid short-term toxicities. However, no matter how careful any treatment is planned, dose is also delivered to normal tissues and organs.

Though not considered as critical during treatment, long-term effects from the absorbed dose due to scatter radiation deposited in areas further from the treatment target, or "out-of-field", may also be of concern. As cancer survival rates improve, it becomes increasingly important to consider the impact this unintended radiation exposure to normal tissue may have on the patients' long-term health and quality of life [4]. Radiotherapy has been implicated as a contributor to late-term toxicities such as second primary cancers [5] and radiation-induced cardiovascular disease (RICD) [6]. In

1

fact, second cancers are the most common cause of treatment-related deaths in long-term survivors of pediatric malignancies [7]. Therefore, minimizing dose to normal tissue due to incorrect dose planning and from scatter radiation is critical, especially for pediatric patients. Children have more radiosensitive tissues and organs and an expected longer life expectancy.

Proton therapy is a relatively new cancer treatment modality that lacks epidemiologic studies of long-term effects. While it theoretically should improve outcomes and early studies seem promising, large epidemiologic studies showing long-term improvements have yet to be conducted. Such studies, however, require accurate estimates of absorbed dose to the specific organs and tissues for individual study subjects allowing the quantification of risk and an assessment of dose-response relationships [8].

It is necessary to create accurate risk models to be able to quantify and judge the risks versus benefits of modern radiotherapy techniques. While population-based models have been developed to calculate risks of cancer incidence and mortality [9] from radiation, there are no such models specifically dedicated for proton therapy treatments. The present work studies and establishes the methods to aid in dose reconstruction of proton therapy treatments including a method to simulate normal tissue dose from active scanning proton therapy. Afterwards, these dosimetric modules are used along with the most recent risk models from NCI and BEIR VII [10] to calculate the corresponding risk from proton therapy treatments for several pediatric patient cases.

1.2   ADVERSE EFFECTS OF RADIOTHERAPY

Two of the most frequent adverse effects of radiotherapy are second malignant neoplasms (SMN) and radiation-induced cardiovascular diseases (RICD). In the United States, children treated between 1970 and 1986 had a 30-year cumulative incidence rate of second malignant neoplasms of 20.5% [11]. And for patients with Hodgkin's lymphoma, testicular cancer, and certain pediatric cancers, SMNs have become a major cause of morbidity and death [1]. Radiotherapy-associated CVDs are a wide spectrum of heart disorders that may result in morbidity and mortality, most notably after Hodgkin's lymphoma and breast cancer treatments [12]. As a result of these growing concerns, the National Council on Radiation Protection and Measurements (NCRP) convened an expert scientific committee in 2011 to assess associations between radiotherapy and SMNs and CVDs [13]. Two major recommendations the NCRP prescribed was:

(1) prioritizing research to include long-term large-scale follow-up of extant cancer survivors and prospectively treated patients to characterize risks of SMNs and CVDs in terms of radiation dose and type and

(2) to construct comprehensive risk prediction models for SMNs and CVDs.

1.3 RADIATION-INDUCED CANCER

Risks of developing cancer are known to be related to several confounding factors such as age, sex, time, and ethnicity, exposure to environmental agents [14], and medical exposures such as radiological scans, nuclear medicine studies, and external beam radiotherapy [15-19]. For most carcinogens, the exposure-occurrence relationship is usually not a simple dichotomy of two outcomes but lies on a probability continuum. By definition, all carcinogens at sufficiently large doses do increase the risk of cancer, and it is generally accepted there is no increase in risk in the absence of any exposure ($D = 0$). Risks of cancer-induction following a radiation exposure is considered stochastic: different people receiving the same amount of radiation dose may or may not develop cancer, but a person receiving a higher dose will have a higher probability of developing cancer [20].

In the common presence of background radiation, and risks of developing of cancers due to other factors, it is difficult to obtain unequivocal evidence of increased risk due to low levels of radiation. Even in the favorable situation in which the baseline risk is relatively well-estimated compared to the risk of the exposed group, the ability to reliably detect small increases in risk associated with exposure requires a large number of exposed individuals at risk. This is because at low levels of exposure, cancer risks associated with exposure are small relative to baseline, or background, risks and comparatively, the increase in observed cancer rates associated with an exposure are small. This requires a large group of individuals to be followed for long periods of time

to provide sufficiently precise and accurate estimates of risk associated with radiation exposure.

1.3.1 Cancer risk estimates

In the present work, absorbed doses and risk estimates are calculated for patients receiving active scanning proton therapy. Absorbed doses are calculated for all organs, and the long-term risk from is calculated based on current risk models. The risk models used in this work are based on those recommended by the National Research Council's Committee to Assess Health Risks from Exposure to Low Levels of Ionizing Radiation. In its most recent report, Health Risks From Exposure to Low Levels of Ionizing Radiation BEIR VII Phase 2 [10], models have been developed as functional relationships between radiation dose and induced cancer for a variety of endpoints, such as lifetime risks of incidence and mortality.

These risk models use data based primarily on the Life Span Study (LSS) cohort of survivors of the atomic bombings in Hiroshima and Nagasaki. The study of these tragic events allowed epidemiologists to investigate the relationship between dose and risks of secondary effects amongst varying populations, people of varying sex and ages, being one of the first studies with such high-quality cancer incidence data [21]. In addition to the LSS, the BEIR VII committee reviewed and incorporated the vast literature on both medically exposed persons and nuclear workers exposed at relatively low doses, epidemiologic studies on mortality [22], and other models for estimating cancer risks from exposures to low level radiation such as those by the United Nations

5

Scientific Committee on the Effects of Atomic Radiation (UNSCEAR) [23] and by the National Cancer Institute (NCI) [24].

The development of risk models for site-specific cancers is limited by current epidemiologic data. For A-bomb survivor data on solid cancers, parameter estimates based on site-specific data are less precise than those based on all solid cancers analyzed as a single group. It is especially difficult to detect and quantify the modifying effects of variables such as sex, age at exposure, and attained age for site-specific cancers [10]. Such risk estimates are subject to several sources of uncertainty due to inherent limitations in epidemiologic data and in the understanding of exactly how radiation exposure increases the risks of cancer in the low-dose regions. In addition to statistical uncertainties, risk may depend on the type of cancer, the magnitude of the dose, the quality of the radiation, the dose-rate, the age and sex of the person exposed, exposure to other carcinogens such as tobacco, and other characteristics of the exposed individual. While a patient may receive more than simply radiotherapy during his or her treatment, this work focuses on radiation received during radiotherapy and therefore only cancer incidence risks due to the radiotherapy are estimated. Additional risks due to other treatment modalities are out of the scope of this work. In addition, to calculate mortality risks of cancer patients, it would be necessary estimate both the curative effect due to the treatment in combination with its secondary negative effects, which is also out of the scope of the current work.

1.3.2 Risk Models

The basic measures used to compare disease occurrence in exposed and unexposed populations are risks and rates. The association between exposure and a secondary effect is aided by statistical models of risks of secondary effects as functions of dose, typically stratified by variables such as sex and age. Model-based estimation provide an efficient way to utilize the information in available epidemiologic data and a means of deriving risk estimates for dose profile combinations of specific cases [10].

Compared to unexposed populations, the elevated risks of exposed populations are manifested by an increase in cancer incidence (and mortality) rates. An *incidence rate, $\lambda(t)$* is a measure of the disease occurrence used in cancer epidemiology referring to new cases of disease occurring among previously unaffected populations. The cancer risk of populations exposed to radiation, such as that from radiotherapy, can be quantified by the difference between the rates of cancer incidence of the unexposed and cancer incidence of the exposed populations. The difference in incidence rates, or the Excess Absolute Risk (EAR) is described by,

$$EAR(t) = \lambda_E(t) - \lambda_U(t) \tag{1}$$

where $\lambda_E(t)$ refers to cancer incidence rate of an exposed population and $\lambda_U(t)$ is the cancer incidence rate of unexposed population.

A second common measure of discrepancy between an unexposed and exposed populations is the Relative Risk (RR), quantified as,

$$RR(t) = \lambda(t)_E / \lambda(t)_U \tag{2}$$

which describes the multiplicative increase in incidence rates associated with exposure [10] and the Excess Relative Risk (ERR),

$$ERR(t) = RR(t) - 1 \qquad (3)$$

relating the exposed and unexposed rates as,

$$\lambda_E(t) = \lambda_U(t)\{1 + ERR(t)\} \qquad (4)$$

Most site-specific cancers have been found to follow a linear dose-response with a few exceptions, such as leukemia, which has been found to be more accurately described by a linear-quadratic model [11, 25, 26]. In this work, however, only cancer induction that use linear dose-response models are considered and described.

In this context, a stochastic linear dose-response model presupposes that the risk of cancer incidence increases linearly with dose. However, the slope of the line, which measures the increase in risk (for a unit increase in dose), has to be estimated from data using the method of maximum likelihood [27]. With linear dose-response functions, the general models for the ERR and EAR using models to calculate the instantaneous risk that a population receives at an age, a, is described as,

$$\lambda_E(c, s, a, b, d) = \lambda_U(c, s, a, b)\{1 + ERR\ (D, a, e, s)\} \qquad (5)$$

and,

$$\lambda_E(c, s, a, b, d) = \lambda_U(c, s, a, b) + EAR\ (D, a, e, s) \qquad (6)$$

where $\lambda_U(c, s, a, b)$ is the background rate at zero dose, and depends on location c, sex s, attained age, a, b is the birth cohort, e is the age at exposure, a is the attained age, and s is the sex identifier.

To calculate the increased risk due to radiation, the *EAR* and *ERR* are calculated as a function of dose an individual receives,

$$EAR \text{ or } ERR\,(D, a, e, s) = D * \beta_s * e^{\gamma e} * a^{\eta} \qquad (7)$$

where D is the dose expressed in Sieverts, β_s, is the ERR or the EAR/10^4 *PY*, a is the attained age, e is the age at exposure, and s is the sex-specific tag. The BEIR VII committee suggests that the *ERR* for solid cancers (except for breast and thyroid cancer) depends on age only for exposures at before 30 years of age, replacing e with,

$e^* = (e - 30)/10$ and is 0 for $e > 30$. The parameter γ gives the per-decade increase in age at exposure for the range 0–30 years. Relevant parameters for ERR and EAR are shown in Table 1.

Table 1. BEIR VII's preferred EAR and ERR parameters for estimating site-specific of solid cancer incidence.

Organ	β_M	β_F	γ	η	β_M	β_F	γ	η
Stomach	0.21	0.48	-0.3	-1.4	4.9	4.9	-0.41	2.8
Colon	0.63	0.43	-0.3	-1.4	3.2	1.6	-0.41	2.8
Liver	0.32	0.32	-0.3	-1.4	2.2	1	-0.41	4.1
Lung	0.32	1.4	-0.3	-1.4	2.3	3.4	-0.41	5.2
Breast		0.51	0	-2		9.4	-0.51	3.5
Prostate	0.12		-0.3	-1.4	0.11		-0.41	2.8
Uterus		0.055	-0.3	-1.4		1.2	-0.41	2.8
Ovary		0.38	-0.3	-1.4		0.7	-0.41	2.8
Bladder	0.5	1.65	-0.3	-1.4	0.2	0.75	-0.41	6
Thyroid	0.53	1.05	-0.83	0				

1.3.3 Lifetime Attributable Risk (LAR) calculations

In this study, the lifetime attributable risks (LAR) are also calculated from proton therapy treatments. The LAR is an approximation of the risk that a radiation-induced second cancer will occur during an exposed population's lifetime. As such, LAR calculations include cancers that would develop without exposure but occur sooner in life because of exposure to radiation. The LAR can be estimated as an time-integral of excess risks for all attained ages (up to the age of 100 years) using either ERR or EAR or a combination of the two [10] :

$$LAR(D, e) = \int_{a=e+L}^{100} M(D, e, a) * \frac{S(a)}{S(e)} da \tag{8}$$

where L is the latent period (5 years for solid cancers) and the ratio $S(a)/S(e)$ is the probability of surviving from the exposed age, e, to age a for the unexposed population, with the $M(D, e, a)$ defined as,

$$M(D, e, a) = EAR(D, e, a) \tag{9}$$

or,

$$M(D, e, a) = ERR(D, e, a) \, \lambda_U^c(a) \tag{10}$$

where the parameter $\lambda_U^c(a)$ is the age- and gender-specific baseline cancer incidence rates at the attained age a [10].

1.4 EPIDEMIOLOGIC STUDIES

One of the most difficult challenges in assessing secondary cancer risks from large epidemiologic studies is that radiotherapy techniques are quickly changing and evolving. These technical advances have greatly impacted dose delivery methods, resulting in dose distributions within the patient that may vary greatly from one treatment modality to another. These improvements have also impacted the likelihood of acute and late radiation-associated toxicities. For example, more conformal techniques have led to better-tolerated treatments with fewer side effects, it may be expected that there are similar impacts on late effects. However, without long-term epidemiologic studies, it is difficult to assess the actual impact.

Despite the lack of long-term studies, novel radiotherapy techniques are being adopted and utilized to treat patients. However, it is critical to use accurate absorbed dose estimates and keep track of patients and investigate the occurrence of short-term and long-term secondary toxicities and morbidities, including quality of life. One of the most notable recent advances in radiation treatment is the increased utilization of proton therapy, which has the ability to concentrate radiation dose in the target volume while sparing normal tissues by reducing exit doses [28-30]. Because it is such a new modality, there is a lack of methods to accurately reconstruct proton therapy treatment dose and assess the risks of long-term adverse effects, such as cancer, that may develop due to the scatter radiation. The methods in this study will be used to both estimate organ dose received from proton therapy and to use the current risk models to calculate the risk of cancer incidence.

Epidemiologic studies investigating the associations of radiation dose on secondary outcomes relies on accurate reconstructions of radiation therapy dose received by the patient during treatment. Because dose estimates are based on patient-specific treatment parameters, the quality of retrospective data depends on how complete and accurate the treatment records are for each subject.

Varying studies will require different methods of dose estimation, depending on the available information and available dosimetry methods. For large epidemiologic studies, there are several methods established to estimate dose from conventional therapy. Many studies reconstructing dose received during conventional radiotherapy utilize the Stovall et al. method [8]. This collection of methods uses various approaches to reconstruct patient dose, such as coupling water phantoms and thermoluminescent dosimeter (TLD) measurements with anthropomorphized anatomies.

Methods used for estimating absorbed dose to organs inside and outside of the defined treatment volume may vary greatly between treatment modalities and may require archival data collection, abstraction and review, and phantom measurements to simulate past exposure conditions [8]. Analytical dose algorithms typically used in treatment planning systems (TPS) provide excellent dosimetric accuracy inside the therapeutic field. In fact, TPS dose may be sufficient for epidemiological studies [31, 32] if the necessary dose is inside the treatment field and there is no complicated heterogeneous anatomy surrounding the region. In such cases, epidemiologic studies of radiotherapy may not require any additional dosimetry.

However, radiation to normal tissue and organ dose outside of the immediate radiation field has only recently been becoming considered to be more and more important due to concerns of long-term adverse effects [13]. Consequently, a growing number of studies now require accurate dose estimates of the areas far away from the tumor area. In these regions, treatment planning systems severely underestimate scattered radiation and are not suitable for research into effects of the low dose radiation in those regions [33]. Since the dose in these regions cannot be estimated with confidence [34-37]; therefore, alternative methods estimating organ dose need to be pursued.

There are three major components of absorbed dose outside treatment beams from external beam radiotherapy which, for conventional radiotherapy are not accurately accounted for in current TPS dose calculations:

(1) radiation leakage through the head of the machine,

(2) scatter off of the beam collimators, and

(3) scatter within the patient from the primary beam [8].

When additional information is available, more accurate dose reconstruction methods, such as Monte Carlo simulations, are used. For example, Lee et al. [38] developed a method to couple computation phantoms and the x-ray voxel Monte Carlo code (XVMC). Joosten et al. [39] calculated organ-specific out-of-field doses after IMRT for breast cancer treatments using whole-body CT scans coupled with in-house Monte Carlo models.

1.5   DOSE FROM CONVENTIONAL PHOTON VS PROTON THERAPY

Conventional external beam radiotherapy concentrates the dose in the tumor while minimizing dose to normal tissue by distributing the dose across normal tissue from different fields. In photon therapy, the dose distribution reaches its maximum in the body near the beam entrance and is then followed by an approximately exponential decrease in dose deeper into the body as shown in the illustrative Figure 1.
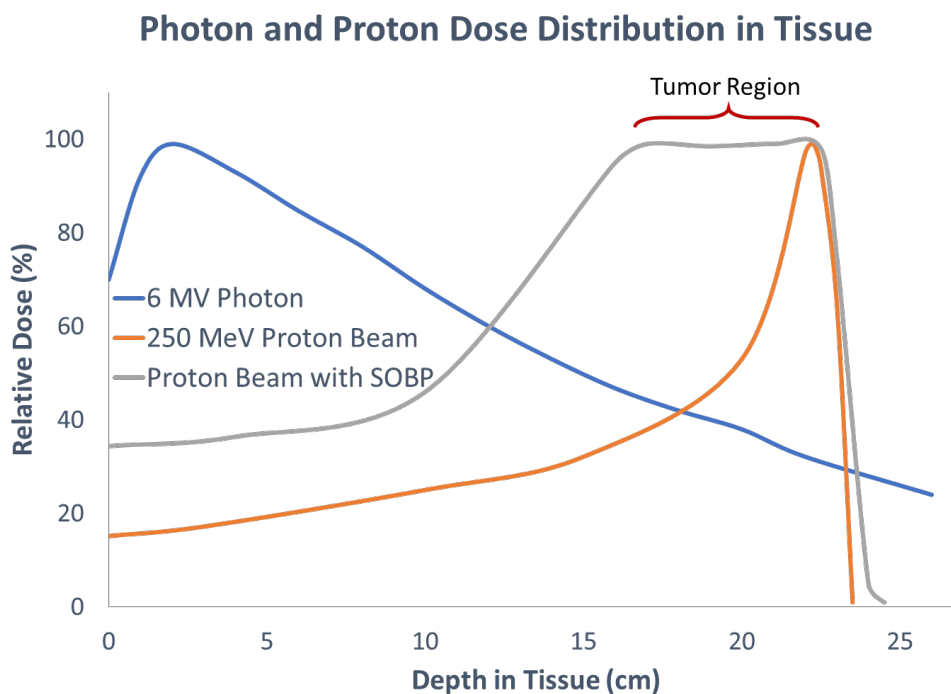
Figure 1. Comparison of dose deposition from an external 6 MV photon beam and an illustrative pristine Bragg peak from a mono-energetic beam and a spread-out Bragg peak (SOBP) from a multi-energy beam treatment.

1.6 ADVANTAGES OF PROTON THERAPY

The advantage of utilizing proton therapy is the potentially improved dose conformation to the tumor and a smaller dose to normal, normal tissue compared to that due to conventional radiotherapy treatments. Due to the physical properties of protons, it is possible to plan treatments with an integral dose that is better than the best conventional treatment modalities. Currently, some of the most common types of these therapies are 3D conformal radiation therapy (3D-CRT), intensity modulated radiation therapy (IMRT), and volumetric arc therapy (VMAT) [40]. Figure 2 is an illustrative figure comparing the dose deposition from a photon therapy treatment plan and one from proton therapy.

Conventional Photon Therapy
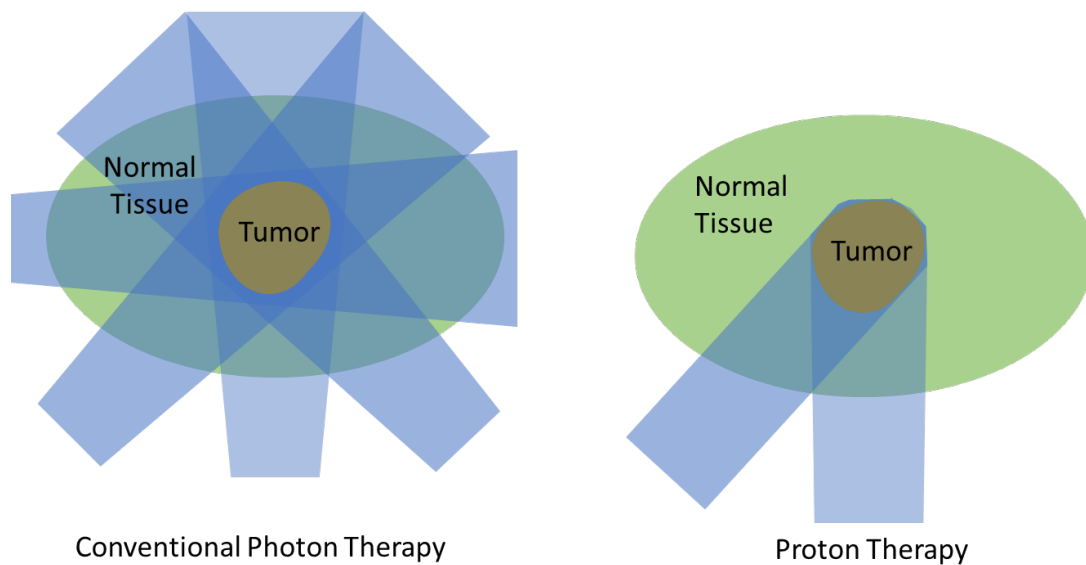
Proton Therapy

Figure 2. Illustrative difference between photon therapy and proton therapy dose delivery demonstrating why integral dose from proton therapy can be as little as a third from conventional photon therapy.

Due of their physical properties and use of fewer fields, integral dose from proton therapy can be as little as a third of that from conventional therapy and a half of that from x-ray IMRT [41]. This is especially of great interest in pediatric patients who, as compared to adults, receive a greater dose to their healthy organs on average due to their physical smaller size [42] and higher sensitivity to radiation-induced cancers by a factor of at least 10 [43].

On average, protons are slightly more biologically effective than photons, with an average Relative Biological Effectiveness (RBE) during treatment estimated to be 1.1 [44]. Therefore, a lower physical dose may be used to cause the same biological effect [45]. Due to the potential benefits of proton therapy for treating solid tumors, it has been growing in popularity and use worldwide. As of November 12th, 2017, there are 26 proton therapy centers in the US and 11 more under construction [46]. In some cases, proton therapy may be the only acceptable treatment in curable children because of its more favorable dose distribution characteristics around a tumor.

However, proton therapy is still a relatively new modality of cancer treatment and it has significant issues to overcome. Moreover, there have not been many epidemiologic studies showing improvements of clinical outcomes in patients receiving proton therapy when compared to conventional photon modalities. This requires immediate attention. Epidemiologic studies looking into long-term effects due to proton therapy and comparing it to late-effects from more conventional photon therapy are in their initial stages at the NCI requiring full body organ dose estimations from novel treatment modalities.

16

1.7   DOSE TO NORMAL TISSUES

Scatter radiation resulting in dose to normal tissues during photon therapy is usually in the form of photons and scattered electrons. However, treatments using very high energy photons can potentially generate neutrons through photonuclear (γ, n) interactions in the patient and accelerator's treatment head [47] and should be considered. Photons require energies greater than 8-10 MeV (~12-15 MV) to physically be capable of producing neutrons and it has therefore been standard to avoid higher-energy treatments. However, for certain cases, they are the best course of action. For example, for breast treatment it has been shown optimal to treat with a combination of 6 MV and 18 MV [48]. With newer treatment methods and increasing interest in low dose received by normal tissues, there has also been growing interest in neutron dose from these high energy photon treatments [47, 49, 50].

During proton therapy, neutrons are always produced and are the main component of secondary scatter dose to normal tissue. As such, for a 70 Gy treatment from a course of proton therapy treatment for pediatric patients, the neutron dose could potentially be equivalent to up to ~30 CT scans [51]. This is due to the fact that whenever protons pass through material and tissues, there is a probability that they will undergo a (p, n) nuclear reaction producing neutrons. And, because neutrons can be highly biologically effective, even a small dose may cause undesired secondary effects in the patient, worst of which is cancer [18]. Following studies into preliminary evaluations of dose being possibly inaccurate – especially in heterogeneous regions – and possible long-term effects from unaccounted secondary particles produced during proton therapy, there has been an

increase in interest of accurate dose reconstruction of dose from protons and secondary

particles produced and creating a dose-cancer induction risk assessment from proton

therapy treatments [18, 52, 53].

During proton therapy, neutron production occurs both inside and outside of the

patient with the number of neutrons produced during a treatment depending on the

amount and type of physical material traversed by the proton on the way to the tumor.

As such, the number of neutrons produced during a treatment varies greatly, depending

on a variety of factors including the proton treatment type, patient anatomy, tumor

location, and the treatment plan.

1.7.1   Secondary Neutron Dose

During passive scattering, the majority of secondary neutrons are produced in the

treatment head [54] while spreading the beam out to meet the tumor-specific

conformality, as is illustrated in Figure 3.
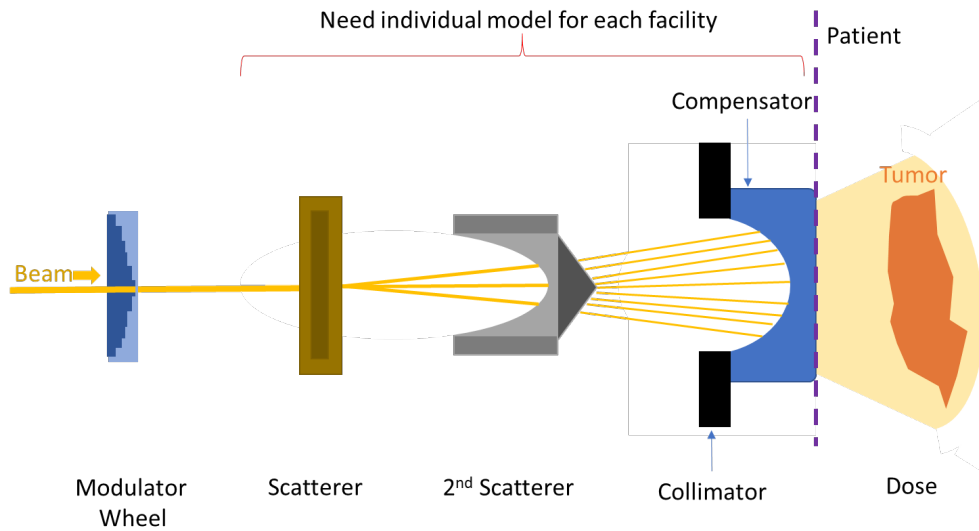
Figure 3. Illustration of typical passive scattering system

Passive scattering methods generate the largest quantity of neutrons by producing them in the treatment nozzle, scattering foils, apertures, and collimators [55]. Neutron dose from such scattering is a growing concern with secondary doses because they may be as high as those from photon therapies such as IMRT [56]. According to previous studies, under passive scattering conditions, secondary neutron dose varies from 0.1 mSv to 8 mSv per delivered proton dose (*Gy*) to the target area. This is affected by the nozzle settings such as beam energy, the scattering material, range modulation, use of snout, aperture, and other additional material.

Modeling passive scattering treatments with Monte Carlo methods therefore requires simulating the full "treatment head". To do this, blueprints and measurements taken at each proton treatment center are needed to create a facility-specific Monte Carlo simulation environment [53, 57]. This is due to the fact while the protons passing through scatterers conform the beam shape to cover a larger treatment, the beam also

undergoes nuclear (p, n) interactions with the material it passes through producing

secondary dose in the form of neutrons. In the treatment head, it is typical for the proton

beam to interact and scatter off of lead, brass, tungsten, and aluminum. A comparison

between the cross-sections for (p, n) in common material used in the treatment head (Al,

Pb, W) and inside the patient (C, N, O) as a function of incident proton energy were

obtained from JANIS [58] is shown in Figure 4.
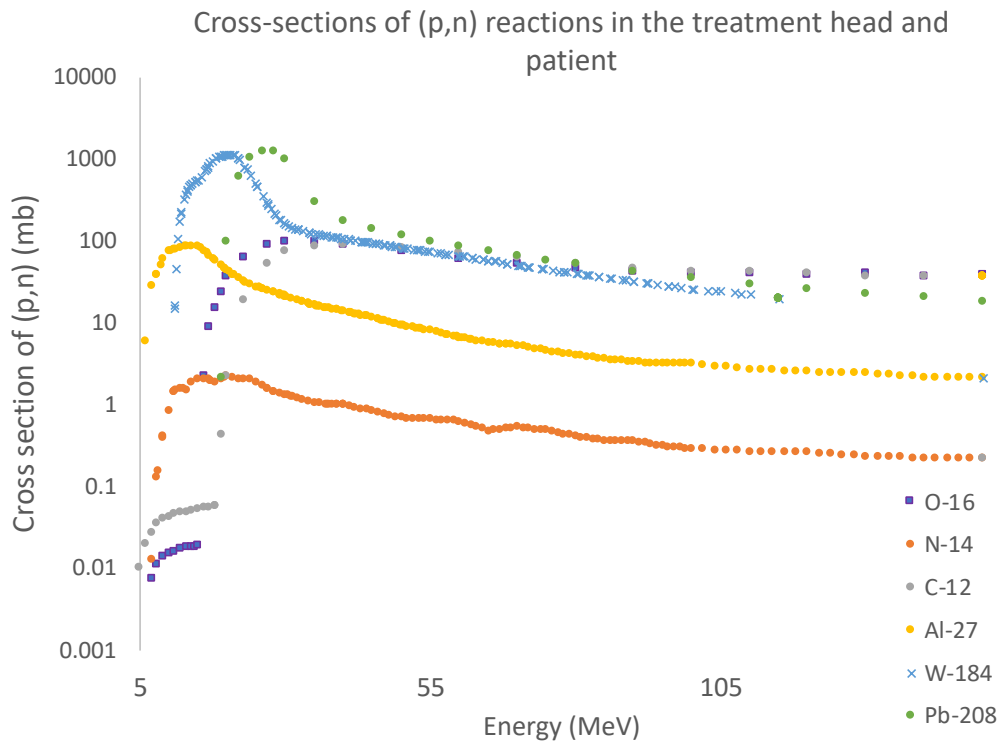
Figure 4. Cross sections for proton-neutron nuclear interactions with elements inside the patient (C, N, O) and external to the patient, from the treatment head (Al, W, Pb).

1.7.2   Active scanning proton therapy

This work, however, focuses on the newer and growing in popularity, active or "spot" scanning method of proton beam delivery. While passive scattering matches the profile of the tumor by spreading the beam out by increasing the amount of nuclear interactions (and neutrons produced), active scanning instead uses electromagnets to direct the proton beam [59] and "paints" the dose, delivering dose pockets or "spots", as is illustrated in Figure 5, increasing proton dose conformality and reducing the secondary neutron dose.
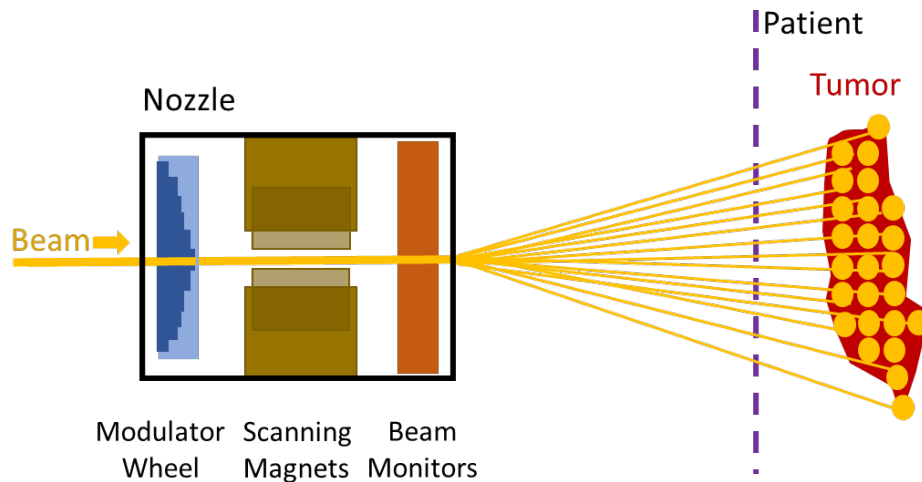
Figure 5. Illustration of typical active scanning system

Though the number of neutrons produced is reduced significantly during active scanning, there are still neutrons produced within the patient. During active spot scanning, the great majority of neutrons are produced within the patient.

1.7.3 Low-dose scatter radiation from proton therapy

Recently there has been growing interest in the dose received by normal tissue in the out-of-field regions from scattered radiation from proton therapy treatments. A growing number of publications have been establishing and using methods to calculate secondary organ dose from proton therapy [17, 32, 52, 53, 60-64] and comparing it to other treatment modalities [39, 65, 66]. As shown previously, protons undergo a different set of physics compared to photons used during conventional treatments resulting not only in a different dose deposition, but also a different set of secondary radiation, requiring a more sophisticated method of dose estimation.

To quantify the dose and risks due to neutrons, several studies have been published showing various experimental and simulation setups. Neutron dose has been shown to be age and stature dependent and to fall off rapidly as a function of distance from the target [42]. At Massachusetts General Hospital, Jiang et. al. [59] simulated organ-specific patient doses due to secondary neutrons during proton therapy utilizing an image-based whole-body voxelized phantom of the Visible Human Project using a Geant4-based Monte Carlo code. Zacharatou Jarlskog et al. [51] calculated dose to organs away from the target using age-dependent phantoms considering eight typical radiation fields allowing for a systematic study of equivalent doses as a function of field parameters showing that neutron doses to specific organs depend considerably on the patient's age and body stature. Neutron dose from proton therapy was compared to secondary out-of-field photon dose from IMRT by Athar et al. [65] using Monte Carlo transport methods coupled with adult and pediatric voxel phantoms.

However, there have still not been any studies on long-term effects due to the low doses that normal, healthy tissues receive. Moreover, there are no established methods to carry out facility and treatment-specific Monte Carlo organ dose reconstruction of proton therapy treatments for large-scale epidemiologic studies. This work investigates and establishes one of the methods to be used in NCI epidemiological studies to reconstruct doses from scanning proton therapy treatments and such method is applied to measurements from the Maryland Proton Treatment Center, creating the facility-specific beam model which can be used for further dose reconstruction of patients at this facility just from the patient DICOM files.

1.7.4   Proton risk calculation studies

While there are no established method for large-scale epidemiologic studies looking into long-term secondary effects for proton therapy patients, there are studies using risk models, such as BEIR VII [10], that estimate the associated risk for developing a second cancer from scatter radiation from proton therapy treatments based on multiple fields, varying treatments, varying age, and other parameters.

In a recent article by Newhauser et al. [67], the estimated risk of second cancer following a craniospinal (CSI) treatment using adult male phantoms was calculated for passively-scattered and scanned-beam proton treatment units. It was found that the total lifetime risk of second cancer due exclusively to stray radiation was 0.8% for the scanned proton beam treatment. Considering the therapeutic and stray radiation fields, the risk of second cancer from intensity-modulated radiation therapy and conventional

23

radiotherapy photon treatments were 7 and 12 times higher than the risk associated with scanned-beam proton therapy, respectively [67].

For a brain treatment with passive scattering proton therapy, the main contributors to the neutron-induced risk have been shown to be neutrons generated in the treatment head, resulting in most lifetime risks to be < 1% for a 70-Gy treatment [55]. A study by Asthar et al. [42] looked into CSI treatments showing that, for an 8-year-old female patient treated with a spinal proton therapy field, the highest radiation-induced lifetime cancer incidence risks were for breasts of 0.71%, lungs of 1.05% and the rectum of 0.60%. For an 11-year-old male patient treated with a spinal field, the bronchi and rectum showed the highest risks with a 0.32% and 0.43%, respectively.

Risks of secondary effects from radiotherapy differ depending on several patient characteristics. Age and gender both need to be considered during treatment. Young patients are subject to significantly greater risks than are adult patients because of the geometric differences and age dependency [42, 55]. In addition, the younger the patient, the higher the dose deposited in critical organs due to neutrons [51]. Because of these factors, the leading risks from radiotherapy for female pediatric patients is breast cancer. For males, the risks of lung cancer, leukemia, and thyroid cancer were significant for pediatric patients. In contrast, leukemia was the leading risk for an adult [55].

1.7.5 NCI planned studies

During treatment, late effects are not the primary concern, as the focus is on "curing" the patient, which is defined as complete remission for 5 years or more by some protocols. However, because of technological improvements resulting in patients living longer, the advantages of proton therapy need to be scrutinized through epidemiologic studies looking at long-term patient benefits, including quality of life. The National Cancer Institute (NCI) plans to conduct such studies, but first needs to develop the capability to calculate out-of-field absorbed doses from proton treatments, on which this work is focused.

The NCI will be conducting multiple studies assessing the long-term effects of proton therapy from multiple proton therapy centers. The methodology described in this section will be used in the future to simulate doses from these proton therapy centers. The use of dose provided from treatment planning systems may not be sufficiently accurate because the algorithms make approximations which may result in uncertainties and do not include out-of-field doses from neutrons [68].

1.8   OBJECTIVES OF THE PRESENT WORK

This work extends the current NCI dose reconstruction methods limited to x-ray radiotherapy by adding active scanning proton therapy dose reconstruction capabilities. The first objective of this work was to overcome a common issue in dose reconstruction studies of lacking full-body anatomy needed for Monte Carlo simulations by combining the available patient anatomy from CT images with phantom anatomy. The second objective was to establish a method to estimate the full-body organ doses received by the patient during proton therapy using the Monte Carlo code, TOPAS. To do this, neutron transport and scatter was validated by comparing results obtained from TOPAS with experimental measurements and with the well-established Monte Carlo N-Particle (MCNP) transport code. Computational tools were established to translate treatment planning system output data into TOPAS input parameter files using measurements from the Maryland Proton Treatment Center. The final objective was to simulate proton therapy on pediatric phantoms and calculate organ dose and to calculate the secondary cancer risk due to proton therapy based on the BEIR VII risk models.

1.8.1   Lack of full patient anatomy

Advances in radiological imaging combined with modern radiotherapy have made the delivery of radiation to the intended target more accurate. Nonetheless, even the most careful treatment planning will still deliver radiation dose to nearby normal tissues. To overcome the challenges of lacking a) efficient dose reconstruction methods for large-scale patient cohorts and b) the lack of full radiological images representing

patient anatomy, Lee et al. [38] developed the methods to reconstruct organ doses for patients undergoing photon radiotherapy using a series of ICRP computational phantoms shown in Figure 6 coupled with TPS and radiotherapy-dedicated Monte Carlo transport methods. These include the use of DICOM images of contoured hybrid computation phantoms and commercial TPS and X-ray Voxel Monte Carlo (XVMC) code for the simulating dose in-field and out-of-field. This work was later extended to use a full, height-and-weight-specific library of phantoms [69].
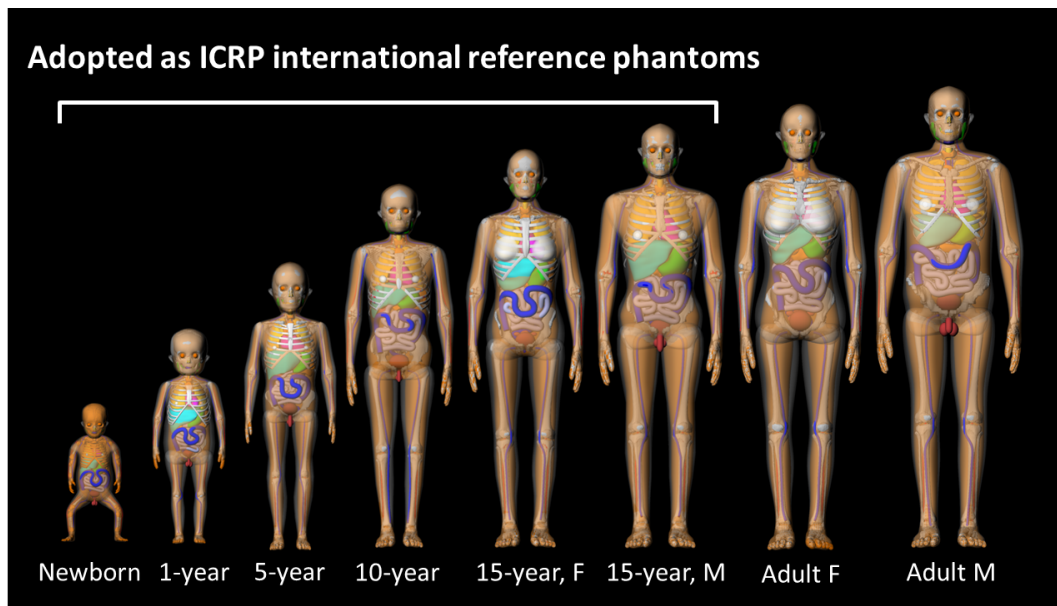
Figure 6. Family of anthropomorphic phantoms with ages ranging from New Born to Adult male and female.

1.8.2   Dose reconstruction from proton therapy treatments

A method to reconstruct doses from proton therapy treatments based on patient data and facility-specific measurements using the Monte Carlo simulation code Tool for

Particle Simulation (TOPAS) [70] is established in this work. The active scanning beam modeling method includes utilizing patient-specific and treatment-specific data for accurate dose simulations. This method will later be extended at the National Cancer Institute to model other proton treatment facilities.

1.8.3   Risk calculation of proton therapy treatments

Risk estimates are often determined from either effective whole-body doses or organ-weighted dose. In fact, the tissue weighting factors used by the NCRP and ICRP for the effective doses are gender-and age-averaged values [13]. However, risk calculations from active scanning proton therapy are carried out on age-dependent, organ-specific risks because baseline risks and cancer occurrences are site-specific. Especially with a treatment such as proton therapy that results in specific regions with high doses within the patient, this may be more meaningful than average total-body risk estimates.

2   METHODS AND MATERIALS

2.1   ANATOMY EXTENSION METHODS FOR OUT-OF-FIELD DOSIMETRY

Improved knowledge of the relationship between organ dose received during radiotherapy and secondary effects is critical for the optimization of treatment techniques and the development of preventative measures for mitigating toxicities. Epidemiologic investigation is one important way to assess the risk of late effects following radiotherapy, and accurate organ dosimetry is a key component of such analysis. Dosimetry for epidemiologic studies, however, poses several unique challenges.

First, the dose calculation methods need to cover regions beyond the target and adjacent tissue which are not often considered as part of standard clinical practice. The methods must also be simple and fast enough so that they can be applied to a large cohort. To address these issues, previous epidemiologic studies have relied on analytical dose calculation methods based on physical measurements in water phantoms [8, 13, 71]. More recently, advanced analytical methods [72, 73] and streamlined Monte Carlo radiation transport methods [38, 74] have been proposed.

Second, for retrospective epidemiologic studies, there is often large uncertainty in the patient anatomy because radiological images are not always accessible for patients who were treated many years ago or may be too expensive to retrieve. Furthermore, even when computed tomography (CT) images are available, it is often the case that the scan coverage does not include all the anatomy of interest. CT scans conducted for

radiotherapy planning typically cover only a portion of the body near the target volume. However, epidemiologists are often also interested in the dose received by normal tissues located further away [75]. The tissues and organs of interest may be located completely outside the CT scan coverage or may be only partially included. One way to overcome this challenge is to use whole-body computational human phantoms [76, 77] which provide extended anatomy for calculating dose to out-of-scan organs. However, there will inevitably be a difference between the anatomy of the computational phantom and the patient. Organ dose calculations need to be highly individualized, and for some applications, small anatomical differences can result in substantial differences in absorbed dose. This is especially true for radiotherapy because of the steep dose gradients involved.

An important research question is how computational phantoms can be adjusted to a specific individual to improve dosimetry methods. It was hypothesized that organ dosimetry estimates can be improved by incorporating partial-body CT images, when available, into the computational phantom. To test this hypothesis, an automated method was developed for extending a partial-body CT to whole-body anatomy for cases where the organs of epidemiologic interest reside outside the available CT scan range. This method was called Anatomically Predictive Extension (APE) and the resulting patient-phantom combination is called an APE phantom.

2.2   ANATOMICALLY PREDICTIVE EXTENSION (APE) METHOD

Anonymized chest-abdomen-pelvis (CAP) CT scans of five patients were retrieved

from the National Institutes of Health (NIH) Clinical Center in Digital Imaging and

Communications (DICOM) format. The in-plane resolution of the images ranged from

0.8203 cm × 0.8203 cm to 0.9375 cm × 0.9375 cm. The slice thickness of the CT images

was 0.5 cm for all patients. The CAP CT scans cover nearly all the organs of

epidemiologic interest starting at the lung apices and extending to the symphysis pubis.

The average age of the five patients was 52 years (45 – 58 years). The average height

and weight were 176 cm (162 – 193 cm) and 85 kg (68 – 104 kg) with the body mass

index (BMI) ranging from 24 to 30 kg/m². The CT images were imported into an Eclipse

treatment planning system for the contouring of major organs. Subsets of the CAP CT

scans were created for testing the APE method, with the full CAP CT scans being used

as ground truth. Two partial-body image subsets were created from the CAP CT scans:

one representing a chest CT (lung apices to cost phrenic angle) and the other

representing an abdominal CT (diaphragm to symphysis pubis).

2.2.1   Computational phantom selection

The APE method substitutes the missing patient anatomy with that of a

computational human phantom selected from a library of phantoms developed at the

NCI in collaboration with University of Florida [69]. The library consists of a total of

351 pediatric and adult phantoms with different heights and weights to represent the US

population. The height and weight of the adult male phantoms ranges from 160 to 190

31

cm and from 50 to 140 kg, respectively. These whole-body phantoms were developed based on patient CT images and contain over 100 different organs and tissues. The polygon-mesh phantoms used in this work were voxelized to match the resolution of the five patient CAP CT scans described above. The voxelized phantoms were then converted to DICOM CT images and a corresponding DICOM-RT structure file containing the phantom organ contours. The methods for generating these files were described in a previous work [38]. For this work, computational phantoms from the library most closely matching each of the five patients were selected based on available data from the medical records such as age, gender (in this study, male), height, and weight. The arms of the phantoms were removed before voxelization to approximate CT patients who have their arms raised above their shoulders (i.e. outside the CT scan range).

2.2.2   Identification of the optimal merge location

An algorithm was developed to automatically select the optimal axial z-position in the phantom where the patient's partial-body CT can be inserted to create an approximately continuous whole-body anatomy. This was achieved by generating two-dimensional anterior-posterior (AP) masks of the patient and phantom skeletal structures. The skeletal masks were created by applying a threshold to the CT image pixels based on their assigned Hounsfield Unit (HU). Pixels in the range of 285 HU to 3500 HU were selected to capture most skeletal structures. The masks were normalized to have a value of 1 in the skeleton and a value of 0 elsewhere.

The optimal merge location was selected as that resulting in maximal overlap between the phantom and patient skeletal masks. A global search is conducted by scanning the patient skeletal mask across the phantom skeletal mask in both the lateral and axial directions. A Dice similarity coefficient is calculated for each possible alignment of the masks. When the upper-left hand pixel of the patient skeletal mask is located at pixel index position (x, z) relative to the phantom skeletal mask, the Dice Similarity Coefficient, DSC, is calculated as,

$$DSC(x, z) = \frac{2N(Ph(x,z) \cap Pa)}{N(Ph(x,z)) + N(Pa)} \tag{11}$$

where, N is an operator yielding the number of pixels of value 1 in a binary mask, Pa the two-dimensional (2D) skeletal mask of the patient derived from the patient's partial-body CT, and $Ph(x, z)$ is the 2D skeletal mask of the whole-body phantom cropped to the size of the patient mask so that the pixel at index coordinate (x, z) is in the upper-left hand corner. The mask $Ph(x, z)$ is padded with zeros as necessary so that it is the same size as Pa. The DSC can range from 0 to 1, where a value of 0 represents the case where masks do not overlap at all and a value of 1 represents the case where the masks overlap completely. The DSC will reach a maximum at some optimal index coordinate (x^*, z^*). The optimal z-position, z^*, is selected as the location for inserting the patient images into the phantom. The optimal lateral coordinate, x^*, provides some information on how to align the skeleton of the patient and phantom in the lateral direction. However, it was opted instead to use the outer dimensions of the patient and phantom for the lateral and anteroposterior alignment as described in the next section.

The reliability of our method for registering the phantom and patient anatomies was evaluated using the five patient CAP CT scans. A total of 23 subsets of the CAP CT image stacks which were 20 cm in axial length were generated at axial increments of 2 cm, starting from the lung apices to the symphysis pubis (0 to 20 cm, 2 to 22cm, 4 to 24 cm, etc.). The optimal merge location for each of the CT subsets was calculated using the method above. The axial position, z^*, selected for the CT subsets was then compared to the expectation that they should incrementally increase by 2 cm (0, 2, 4, 6 cm, etc.) as constructed for the five patients.

2.2.3   Merging patient and phantom anatomy

The patient and phantom anatomies are merged at the selected axial position z^* by overriding the phantom anatomy with that of the patient. A bounding-box registration method was used to reduce discontinuities between the phantom and the patient. The phantom portions are linearly scaled in the lateral (x) and anterior-posterior (y) direction to match the outer contour dimensions of the patient as measured on the first and last image in the patient's partial-body CT stack. The phantom image stacks appended above and below the patient's partial-body CT image stack are scaled independently and aligned at the center of the bounding boxes.

The tumor and the selected organs at risk in the patient are typically contoured by manual segmentation as part of the radiotherapy treatment planning. The phantoms used in this work have the advantage that they come pre-contoured with over 100 different organs and tissues. Our anatomy extension method reads the pre-existing DICOM-RT

34

structure files of the patient and combines them with those of the phantom, overriding the phantom contours where necessary. The patient and phantom structures are matched through the use of standard naming conventions. The same translation and scaling factors applied to the phantom images are applied to the phantom contours. For instance, the upper half of the patient's liver may be contoured from the partial-body CT images. The lower half of the liver will then be taken from the phantom and the two structures will be combined into a single liver structure in the final merged APE phantom.

2.2.4 Automated scripts for anatomy extension

An in-house application was written in the Python computer language to automate the APE method. A key feature of this software is that it reads and writes files in DICOM format. The input to the software is the patient's partial-body CT and a corresponding DICOM-RT structure file containing the patient's radiotherapy target and normal tissue contours. The output of the software is a directory containing the DICOM CT images of the whole-body APE phantom and a DICOM-RT structure file containing the APE phantom organ contours. These files can then be used as the input for dose calculation tools such as a commercial treatment planning. The workflow of the APE method is summarized in Figure 7.
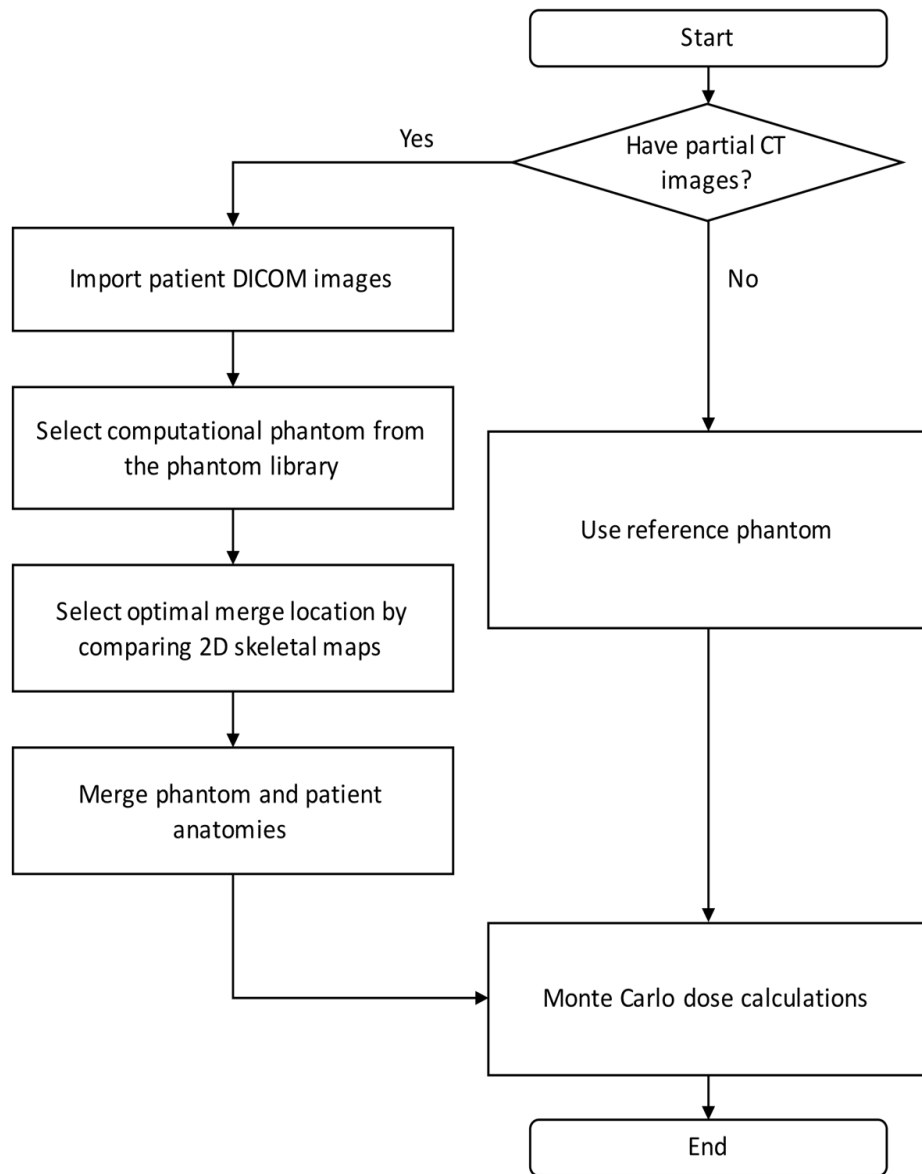
Figure 7. Workflow of the anatomically predictive extension (APE) method.

2.2.5 Validation of APE Method in illustrative radiotherapy

When a patient's CT images are unavailable, and height and weight are unknown, the best option for dose reconstruction is to use a reference phantom as a surrogate for the unknown anatomy. In this work, my aim was to test whether the organ doses calculated using APE phantoms would be more accurate than those calculated using a reference phantom. Two idealized cases representing chest and prostate radiotherapy treatments were considered. Organ doses were calculated for simple chest and prostate irradiations that were planned on a reference computational phantom [78] (assumed patient geometry if no CT images are available), the APE phantoms (patient-phantom hybrid given a partial-body patient CT), and the full patient CAP CT images (ground truth).

As the normal tissues of interest are located away from the primary radiotherapy fields, a methodology to calculate out-of-field organ dose that was previously published by the Radiation Epidemiology branch was selected [38]. This method uses the X-ray Voxel Monte Carlo (XVMC) code as the dose calculation engine [79]. All cases were transferred to an Eclipse treatment planning system. A certified medical physicist created simple chest and prostate treatment plans on the patient CAP CT scans (Figure 8). The same treatment plans were then copied to the reference phantom and APE phantoms. The mean organ dose received by the heart, left and right lungs, liver, stomach, bladder, and prostate was calculated for the idealized radiotherapy treatments. Sufficient particle histories were simulated to ensure that the Monte Carlo statistical error on the organ dose estimates was negligible (<1%) in all cases.

37
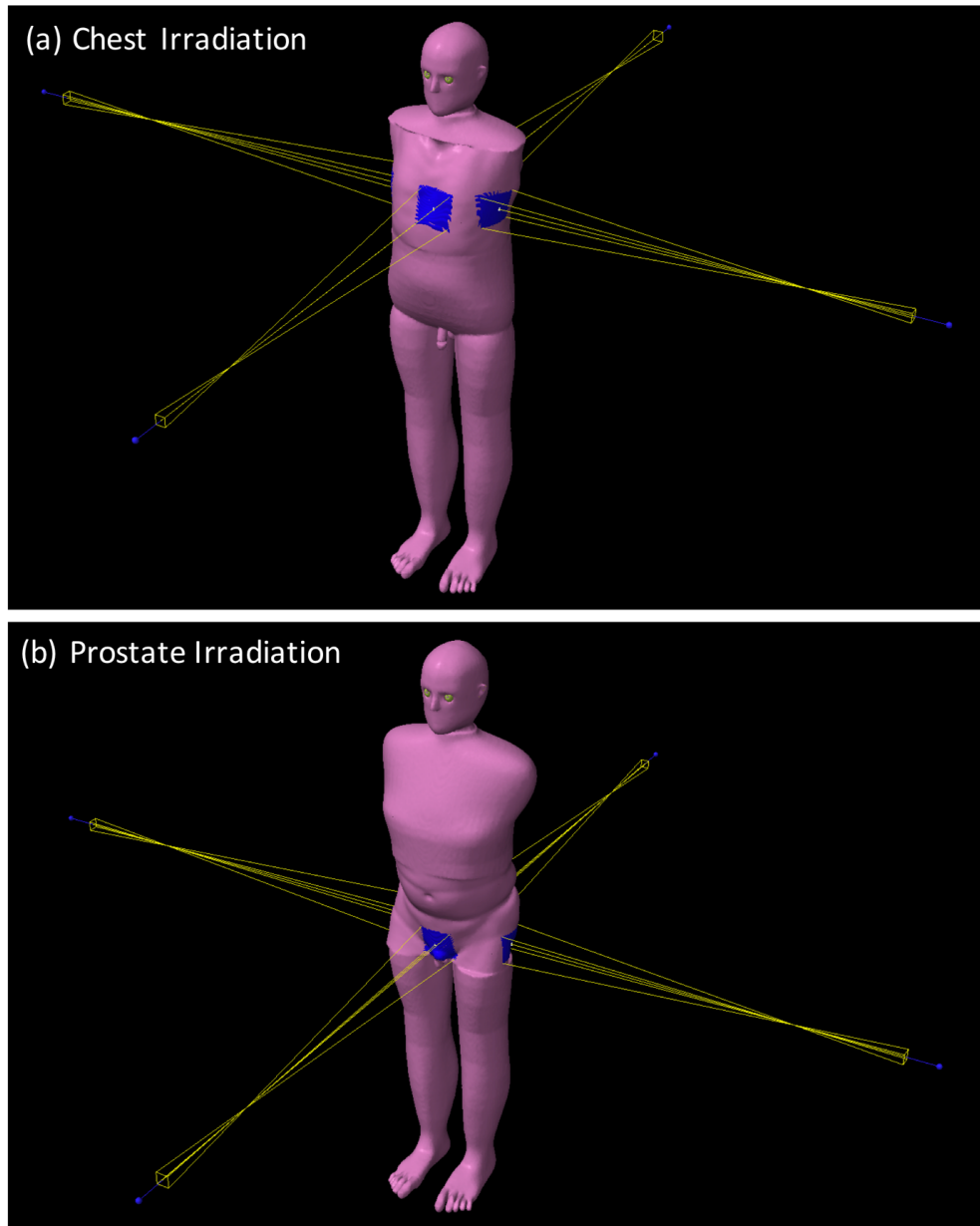
Figure 8. Screenshots of the chest irradiation (a) and prostate irradiation (b) taken from the Eclipse treatment planning system.

2.2.6 Patient CT and selected phantoms

Figure 9 shows the chest and abdominal CT images extracted from the CAP CT scans of the five patients having different heights and weights. The body size-matched adult male computational phantoms are shown to the left of the patient CTs in increasing order of BMI.
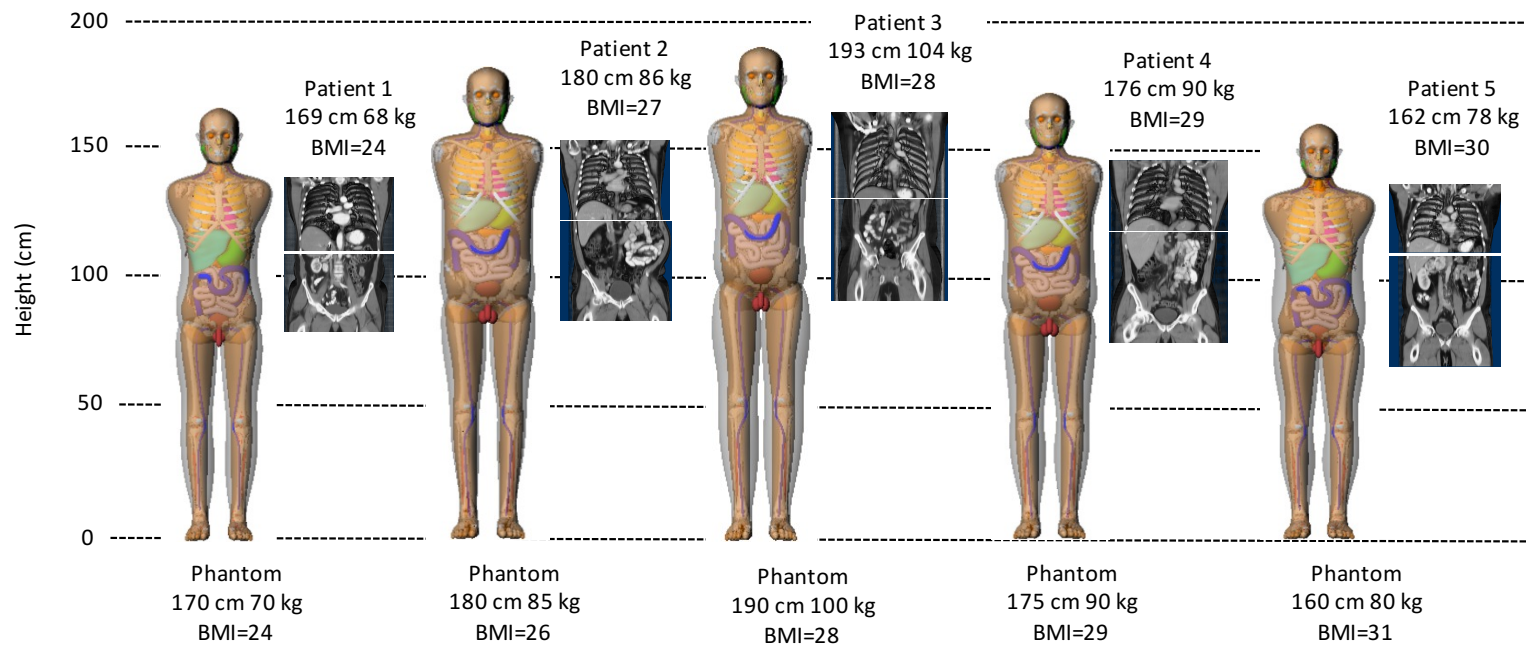
Figure 9. The chest and abdominal CT image sets extracted from the full chest-abdomen-pelvis (CAP) CT scans for the five patients. The patients have different BMIs which range from 24 to 30 kg/m2. To the left of the patient images are the computational.

2.2.7   Selection of optimal merge location

The performance of the algorithm for determining the optimal merge location for the five patients is shown in Figure 10. The distance between the lung apices of the patient and the top of the partial-body CT extracted from the CAP scans is plotted on the x-axis and increases from 0 to 44 cm in 2 cm increments. The corresponding optimal merge location, z^*, for each subset of the CAP scan are shown on the y-axis relative to the axial location of the lung apices in the phantom. We expect that the graph would show a line to identity if the algorithm perfectly maps the patient skeletal anatomy onto the phantom. Overall, the selected merge locations for the five patients show good agreement with the original anatomical locations. As the mapping process is based on the bony structures, we found that it is sensitive to the postures of the patients and phantoms. The least accurate portion is in the 0 to 10 cm range, which is attributed to differences in scapular rotation. The patients have their arms positioned above their shoulders, while the phantoms originally had their arms down at their side. The slope of the lines in Figure 10, do deviate from 1. This indicates that even though the patient and phantoms have similar heights, there can still be systematic differences in the distances between skeletal landmarks.

Figure 10. Comparison of the distance of the partial CT skeletal mask (x-axis) with the distance of the merge location selected by the APE algorithm (y-axis) for the five patients.
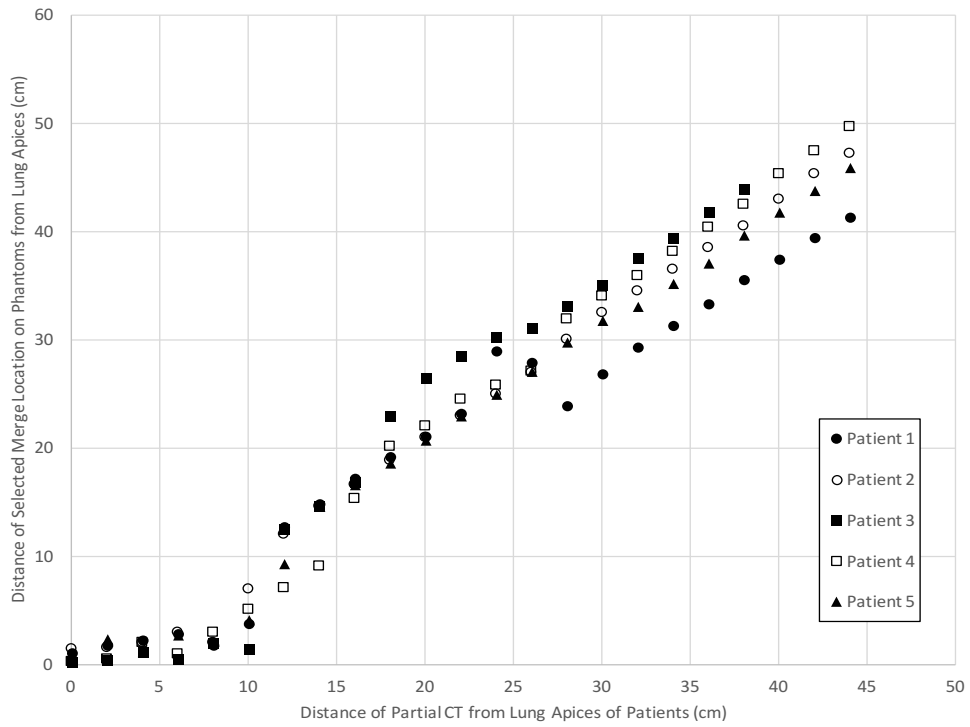
The skeletal mapping procedure for Patient 3 with a height of 193 cm is illustrated in Figure 11. Convolution of the skeletal maps of the chest CT and the whole-body phantom was performed and the largest DSC was calculated as a function of axial position z is plotted on the left in a solid line. The global maximum DSC was 0.66 at an axial position of 162 cm measured from the feet of the phantom. The case of the abdominal CT (Figure 11) had a global maximum DSC of 0.78 at an axial position of 125 cm. In both cases, the DSC reached local maxima at different axial positions (e.g., around 120 cm, pelvis region, for the chest CT and around 175 cm, clavicle region, for the abdomen CT) indicating that this algorithm cannot resolve this issue.
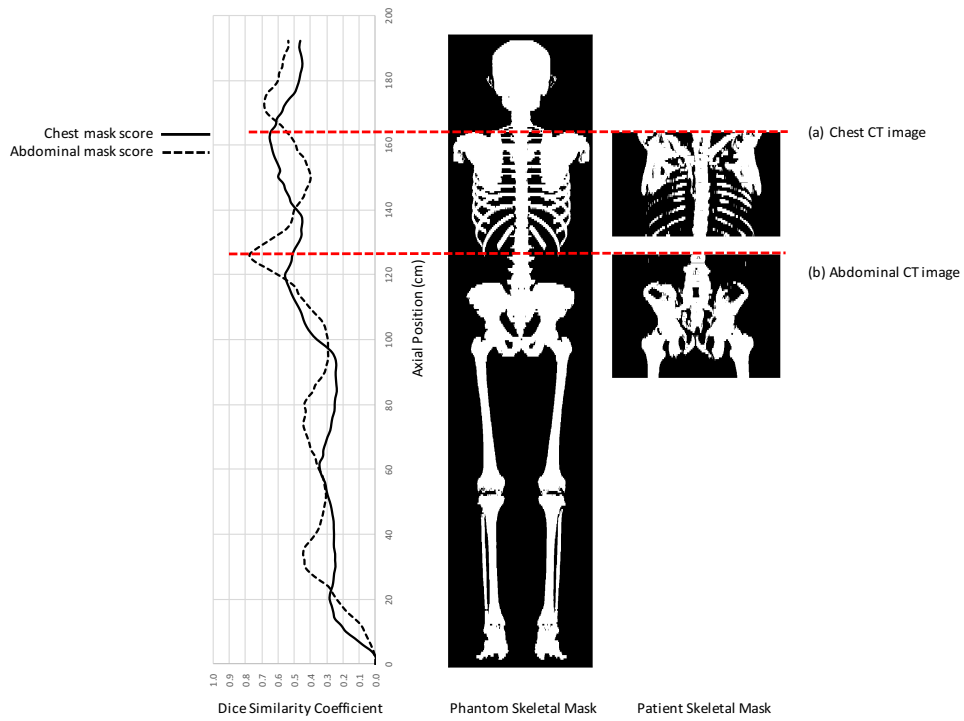
Figure 11. An example of the mapping process for Patient 3. The largest Dice Similarity Coefficient, *DSC*, calculated as a function of the axial position (left), the skeletal mask of the selected phantom (center), and the skeletal masks of patient for the chest (a) and abdominal (b) cases.

2.2.8   APE whole-body phantom

An example of APE phantoms generated from chest and abdominal CT scans take from the full CAP CT scan of Patient 5 is shown in Figure 12. The organ contours for the patient and APE phantom are also shown. The organs at the boundary between the anatomies of the patient and the phantom (such as the liver and the stomach) show imperfect, although sometimes remarkably great, continuity. The organ contours for the patient and phantom are combined so that the mean dose received by the merged organs (e.g., the liver or stomach) can be calculated.
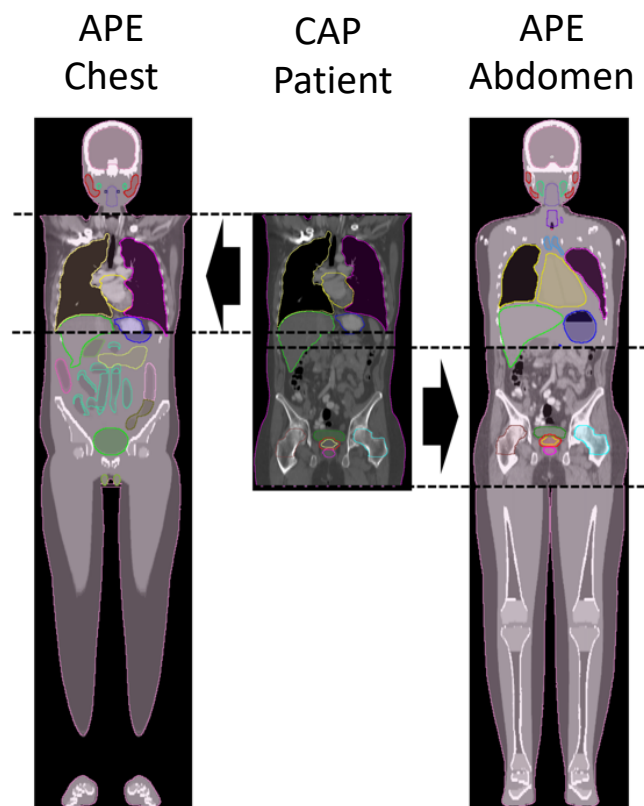
Figure 12. Example APE phantom generated from chest and abdominal CT scans for Patient 5. The chest CT-based APE phantom (left), the original full torso CT of the patient (center), and the abdomen CT-based APE phantom (right).

2.3   MONTE CARLO DOSE SIMULATIONS

It has been shown that Monte Carlo simulations, though computationally more expensive, are greatly superior to analytical methods for dose calculations of x-ray [80] and especially for particle treatments such as protons [81]. In addition, the use of Monte Carlo simulations is needed because TPS may be highly inaccurate in heterogeneous regions [38], does not calculate out-of-field dose, and does not account for neutrons. The Tool for Particle Simulation (TOPAS) Monte Carlo platform [82] has been chosen because it is specifically designed for proton therapy and other radiation therapy simulations. The underlying GEANT4 has been tested and is well-benchmarked [83-88]. However, it has many components and settings making it important to validate TOPAS as a whole to confirm its accuracy, especially in particle scatter and out-of-field dose. While working on validating TOPAS, it was also necessary to work with the developers to fix underlying issues with TOPAS.

In the following sections, particle scatter simulations from TOPAS are compared with measurement and a more established neutron transport code and a generic method is investigated to be used in epidemiologic studies that requires reconstructing dose from facility-specific active scanning proton therapy treatment. Then, a beam model for the Maryland Proton Treatment Center (MPTC) proton beam facility is created, organ doses are calculated for two treatment plans, and the associated risks are calculated.

2.3.1 TOPAS simulation environment

The number of processes, models, and cross-section data available in GEANT4 makes it not only extremely flexible but also a very complex tool to configure. TOPAS has been chosen as the package to best simulate proton therapy treatments [70] because it was designed specifically for particle therapy simulations and its ease of use. There are numerous versions and GEANT4 parameters that can be adjusted, depending on the application type. For these studies, the TOPAS simulation was based on *Geant4 v10.2.p01* using the default settings of TOPAS combined with settings based on Zacharatou et al [89]. This includes the physics list containing the Geant4 modules: *g4em-standard_opt4*, *g4h-phy_QGSP_BIC_HP*, *g4decay*, *g4ion-binarycascade*, *g4h-elastic_HP*, and *g4stopping*. The *QGSP_BIC_HP* portion of the physics list uses GEANT4 binary cascade for neutrons with energies below 10 GeV along with the data driven high precision neutron package, *NeutronHP*, to transport neutrons below 20 MeV down to thermal energies. These physics settings were the same for all calculations in this dissertation work.

2.3.2 Benchmarking TOPAS scatter simulations

The biggest concern for long-term effects resulting from scatter radiation produced during proton therapy is dose from scattered neutrons [90], which may travel far from the target site and have varying energy and relative biological effectiveness (RBE). The RBE of neutrons is dependent on the neutron energy [91], and therefore how TOPAS simulates neutron scatter also needs to be benchmarked. To do this, TOPAS

simulations were created using a simple geometry setup, compared experimentally and with Monte Carlo N-Particle code (MCNP). MCNP is a well-validated, general-purpose code that is used for the transport of particles and has been applied to a multitude of areas such as radiation protection and dosimetry, detector design, radiation shielding, medical physics [92].

A simple geometry was developed to be simulated in TOPAS and MCNP, and to be physically measured at the National Institutes of Standards and Technology (NIST) in Germantown, Maryland. The setup includes a neutron source, a cylindrical phantom, and detectors to be placed centered in phantom and irradiated with a neutron source as shown in Figure 13.
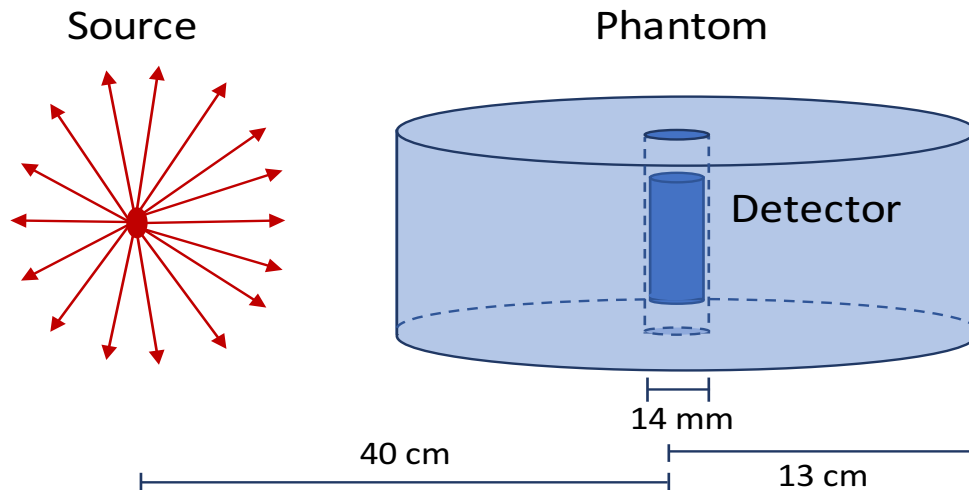
Figure 13. Setup for validation TOPAS scatter simulations. 1) Proton simulations: source monoenergetic, 150 MeV and ICRP adipose tissue phantom; and 2) Neutron simulations: Californium-252 source and polyethylene phantom.

48

For the neutron source, an isotropic NIST Californium-252, minimally moderated with D2O. The emission rate of the source on 2/25/2016 was 1.762E7 n s^{-1}, producing a dose equivalent rate of 0.7662 mSv/hour at 50 cm. A Cf-252 source has an average energy of 2.3 MeV. To recreate the spectrum with simulations, an unmoderated Cf-252 neutron energy spectrum was obtained from ENDF/B-VII. The Neutron Sources and Neutron Dosimetry Calibrations group at NIST also provided MCNP simulation results for the lightly moderated source, as can be seen in Figure 14, comparing a moderated and unmoderated spectrum at 50 cm for the source. This comparison confirmed that the neutron spectrum as measured by the bubble detectors from a moderated source would be indistinguishable from that of an unmoderated Cf-252 energy spectrum.
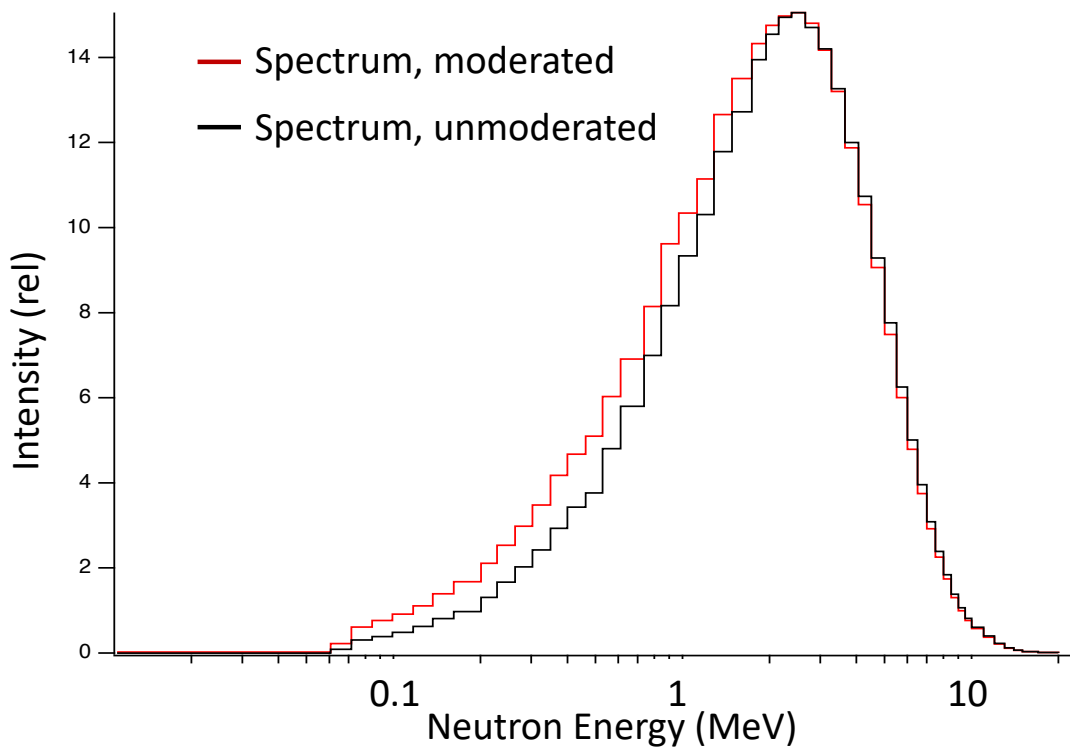
Figure 14. MCNP simulations of the neutron spectrum at 50 cm from the source, showing that the lightly moderated and unmoderated spectrum differ less than the bubble detectors could account[*]

Though several detectors provide better energy resolution, bubble detectors [93, 94] were chosen for these measurements because of their insensitivity to gammas, ability to provide a neutron spectrum, and their small size lending them to provide good spatial resolution. This potentially allows them to be used for providing a neutron energy spectrum with in-phantom measurements utilizing anthropomorphic phantoms for the neutron energy range that is most biologically effective. Each bubble detector (shown in

---

[*] MCNP calculations were performed by members of the Neutron Sources and Neutron Dosimetry Calibrations group at NIST.

Figure 15) has one of 6 different energy thresholds (10 keV, 100 keV, 600 keV, 1 MeV, 2.5 MeV, and 10 MeV) with sensitivities ranging from 4 μSv and 17 μSv.
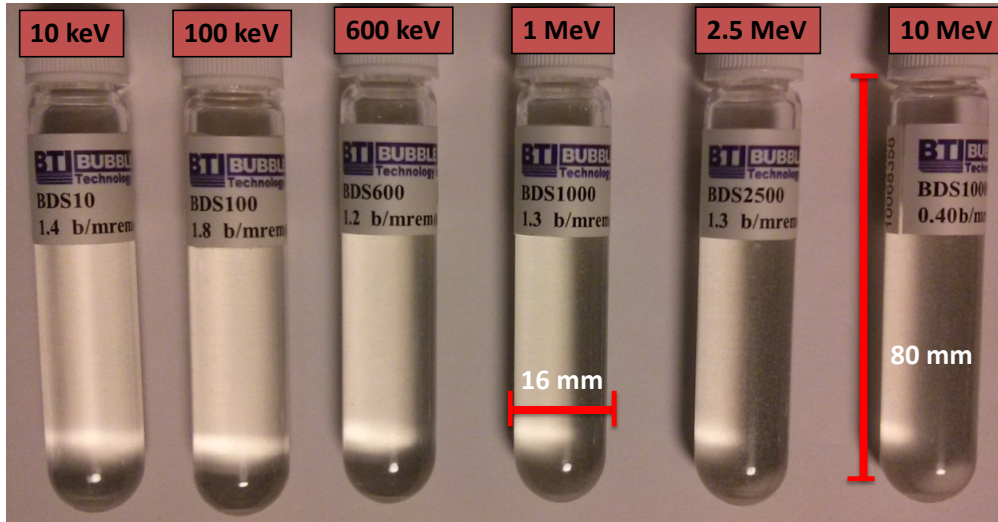
Figure 15. Bubble detectors with varying energy thresholds used for neutron energy spectrum measurements

To measure the scattered neutrons using bubble detectors, each detector needed to be irradiated individually inside the phantom, with each irradiation resulting in at least 300 bubbles in each energy bin for appropriate statistics. To acquire the data, 16 irradiations were completed, each taking from 1 to 63 hours with the experimental setup is shown in Figure 16.
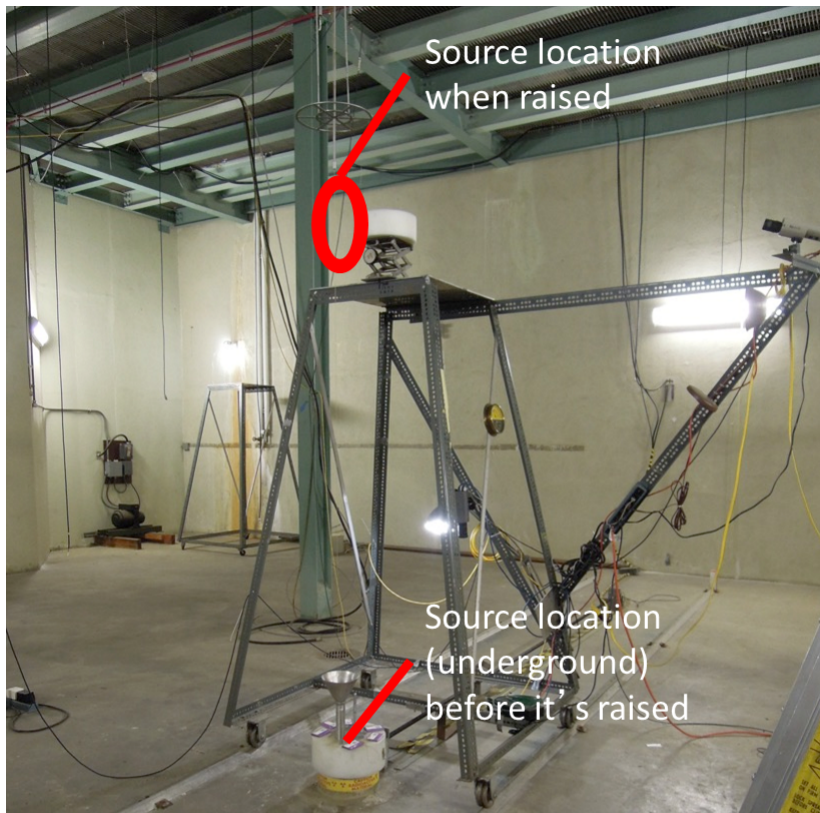
Figure 16. Experimental setup at the National Institute of Standards and Technology showing the source at its position before it is raised for irradiation.

The experimental setup was recreated within TOPAS, as shown in Figure 17, as well as MCNP6. In both simulations, an isotropic neutron source with the spectrum from ENDF/B-VII was placed at 40 cm from the center of the detector and was simulated as a tissue equivalent cylinder inside of a polyethylene phantom. A total of 1 billion particles were simulated in TOPAS by the author and 5 billion particles were simulated using MCNP6 by Dr. Matthew Mille at the NCI.

For the MCNP simulations, neutrons were simulated running in mode *n* using a Californium-252 source modeled using the previously mentioned neutron spectrum and the *poly.20t S(alpha, beta)* data library [95]. The analog energy limit was set above 20

MeV, so in effect, analog capture was always used. The cross-sections from *ENDF71x* Library based on *ENDF/B-VII.1*–Based Continuous-Energy Data Tables [96] were utilized. The TOPAS environment is described in the previous section and shown in Figure 17.
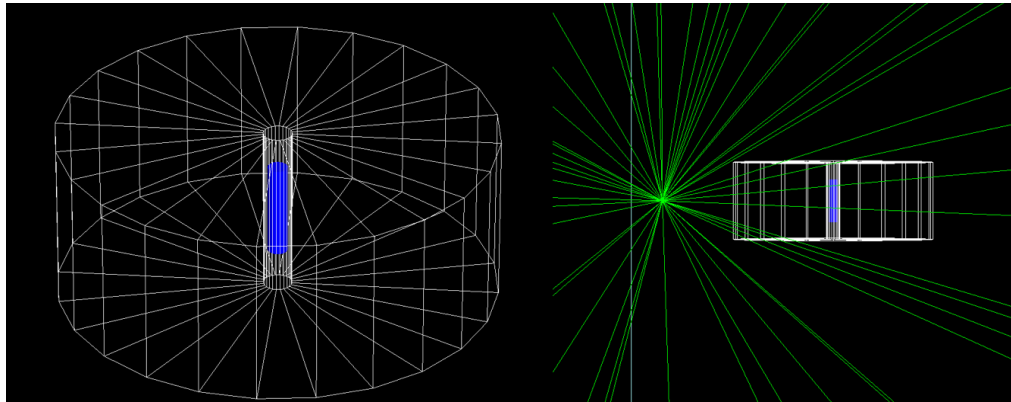
Figure 17. TOPAS simulation reproducing the experimental setup.

2.4 PROTON THERAPY TREATMENT MODELS

2.4.1 Proton therapy dose reconstruction

The National Cancer Institute (NCI) will be conducting large-scale epidemiologic studies to assess the long-term adverse effects due to proton therapy treatments and will be investigating data from multiple proton treatment institutions. The methodology described in this section will be used in the near future to aid in the dosimetry portion of such studies. Passive scattering and active scanning are two of the most common proton therapy treatments modalities used today and due to the difference in dose delivery, separate simulation methods are required. The NCI epidemiologic studies will analyze dose estimates from both scattering and scanning modalities, though the current work focuses solely on developing and investigating method to establish Monte Carlo models of active scanning proton therapy facilities utilizing already available reference data from each treatment center.

For passive scattering, it is necessary to simulate beam interactions in the nozzle because the spreading, modulation, and shaping of the beam are fully determined by the different elements that the beam encounters in the nozzle. In contrast to passive scattering, during active beam deliver, only a few elements are present in the nozzle and they do not significantly contribute to secondary scatter radiation. For this reason, it is possible to model active scanning using two different approaches. The first approach to model the beam includes using blueprints and making measurements to create models of the full treatment head as is shown in Figure 18 (A). However, as mentioned previously, there are few elements in the nozzle that modify and interact with the proton beam, and

therefore the beam can also be modeled starting at the nozzle exit, as is shown in Figure 18 (B). Such models have been created at certain institutions by simulating the interaction of the proton beam in the treatment head and similar models have been proposed for MCNPX [97] and GATE [98].
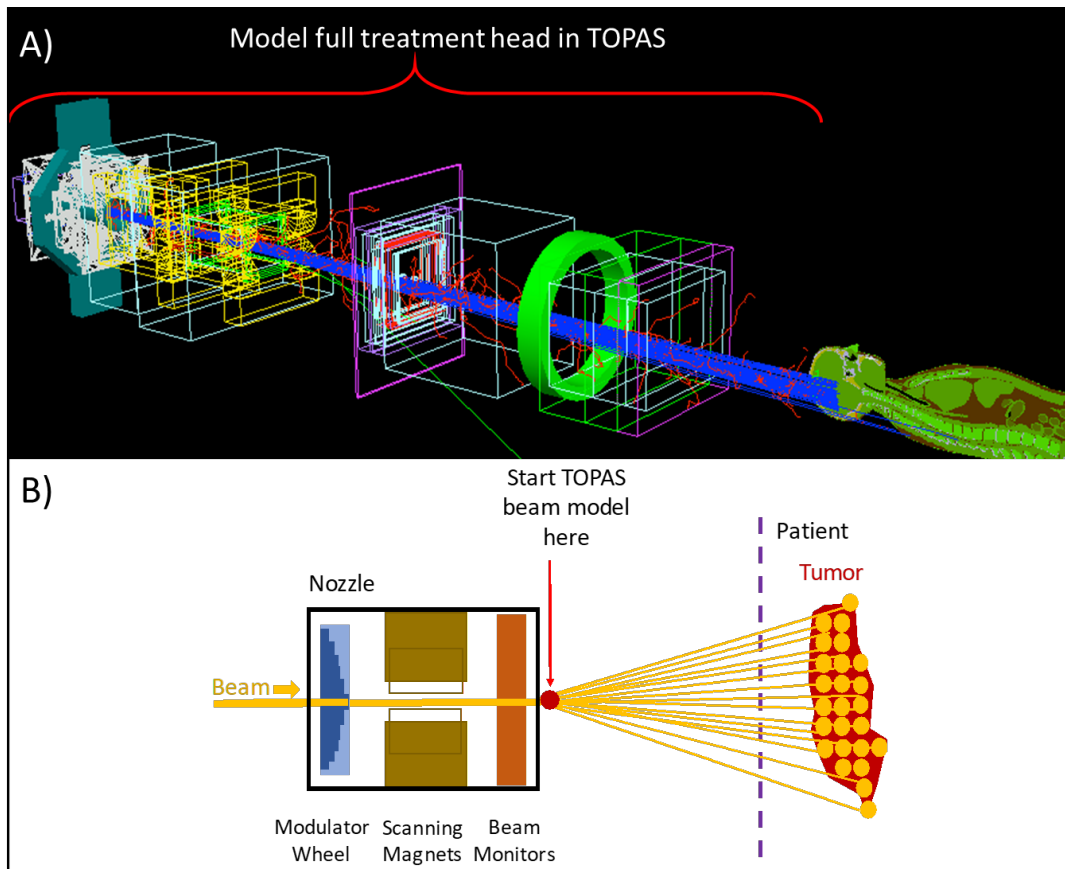
Figure 18. Modeling proton therapy in TOPAS with A) modeling full treatment head and B) modeling the beam after it exits the nozzle.

To act as a pilot study, this work focuses on developing and applying method (B), establishing a beam model for the Maryland Proton Treatment Center facility in

Baltimore, MD using their reference beam data used in commissioning of their treatment planning system (TPS). In future studies, this will be applied to multiple proton therapy treatment centers, from each facility using patient-specific treatment DICOM without requiring blueprints from the facility or extra measurements.

2.4.2   Active scanning proton therapy dose reconstruction modules

To reconstruct dose for epidemiologic studies of proton therapy treatments from multiple institutions, it is first required to establish a Monte Carlo model of each treatment facility and then recreate the treatments at those facilities using the facility-specific models in combination with patient-specific treatment data. This work establishes a generic method to recreate facility- and patient-specific proton therapy treatments and acquire organ dose for each patient. The method is based on those described by Grevillot, et al. [98] and Grassberger, et al. [99] by using reference measurements typically available at each treatment facility.

These described methods were implemented using Python modules to process input patient DICOM data, combined with parametric functions created from reference measurements. Modules then create input parameter files, and additional modules post-process the TOPAS output to provide organ-specific dose and statistical information. The whole process is shown in Figure 19.
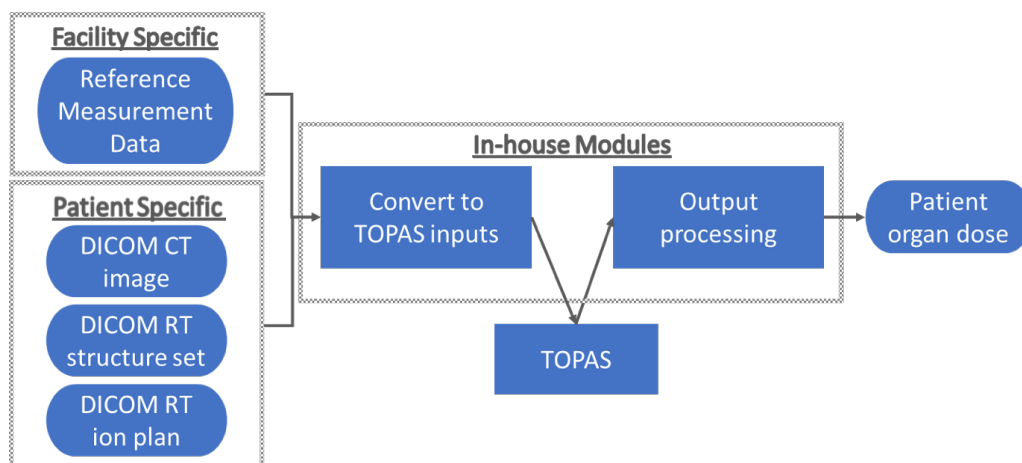
Figure 19. Flow chart demonstrating the proton treatment simulation method using patient treatment plans and typically-available reference measurements.

2.4.3   Facility specific modules

Simulations of facility-specific active scanning treatment plans require modeling the dose delivered to the patients using many individual "pencil beams" based on measurements from those facilities. A proton therapy treatment can have anywhere from tens to thousands of individual proton beams delivering dose in small dose "pockets" typically described as "spots" [99]. To create Monte Carlo simulations using only reference measurements, requires matching the beam output from the simulation to that of a specific facility. This includes matching the optical and energy distribution properties, along with calculating the number of protons necessary to deliver the prescribed dose. This is done using easily-available reference measurement data from the proton treatment facility obtained during the commissioning or part of routine quality assurance/quality control.

Creating these functions characterizing the proton beam for a single facility is an extensive and a time-consuming pursuit. However, this is a necessary procedure to establish accurate dosimetric treatment models to utilize in large-scale studies of proton therapy. To assess the dose received by the patients at each facility, each patient treatment plan is converted to Monte Carlo input parameter files. The treatment plans prescribe the necessary beam energy, beam size at the nozzle exit, and the position of each "spot". Each individual beam is characterized by its energy distribution and optical properties. In this work a method is established to recreate facility-specific proton therapy treatments using the Monte Carlo simulation package, TOPAS [70] and is applied to the data from the Maryland Proton Treatment Center.

2.4.4   Range and energy distribution matching

Measurements commonly found at facilities include integral depth dose (IDD) curves in water phantoms. These curves are measured for specific energy ranges. The same energy values are then simulated in the TOPAS Monte Carlo code recreating each depth dose curve in order to match the ranges. The range, $R90$, is defined as the position of the 90% maximum of the curve in the Bragg peak distal fall-off along the beam path. The energy spectrum is considered to be Gaussian with a mean nominal energy, E_0, and standard deviation, σ_E.

Functions are created to match the simulated energy and distribution at the beam nozzle exit to that of the treatment facility. This tuning is done by first, simulating the proton beam with the energy matching the prescribed energy and comparing the

simulations' dose deposition with that from measurement. Then, the simulated energy is iteratively adjusted until the peaks of the curves from the measurement and simulation match. From the difference between the energies necessary to match the peaks, a function is created to adjust the TPS-prescribed energy for each beam.

Then, the same is done with the energy distribution. To compare the two, the depth dose is first normalized by the area under the curve calculated between depths 0 cm and the corresponding *R90* for each energy. The energy distribution, σ_E, is incrementally and iteratively adjusted. After each adjustment, the simulation is rerun, and the depth dose curve is checked to make sure that the curve matching is improving. After the best-matched sigma is found for each measured energy, a function is also created to estimate the most appropriate σ_E for each nominal energy, E_0, approximating it with the polynomial [98],

$$\sigma_E(E_0) = \sum_1^n a_i * E_0^i \tag{12}$$

with a_i being the polynomial coefficients and E_0^i the nominal energy.

2.4.5   Modeling beam optics

Modules are also created to calculate the optical properties of the proton beam. These are described by the beam size, $\sigma_u(z)$, beam divergence, $\sigma_{div,u}(z)$, and the beam emittance $\epsilon_u(z)$ along the beam path, defined as +z. These modules are based on the nominal energy, E_0 to calculate the beam divergence. To match the optical properties of the TOPAS simulation with that of the treatment facility, reference beam size

59

measurements around the isocenter are typically available for the same energies as those used to match the dose for the IDDs.

At any position along the beam path (defined as the $+z$ axis), the probability density functions of protons in the x-and y-planes follow normal distributions. At a position, z, the beam size is defined as σ_x in the x-axis, σ_y in the y-axis, following the Gaussian function,

$$pdf(u,z) = \frac{1}{\sigma_u\sqrt{2\pi}}e^{-\frac{1}{2}\left(\frac{u}{\sigma_u}\right)^2} \tag{13}$$

where σ_u is the standard deviation of the Gaussian in the x- or y- axes and u is the lateral distance from the isocenter in the x- or y- directions.

The beam divergence, or angular spread distribution, describes the change in spot size with distance along the beam path. To match the beam divergence, in-air reference measurements are taken around the isocenter. Although, due to the intrinsic properties, the beam size should be smallest at the isocenter, the spot sizes actually keep increasing away from the nozzle exit because the beam is also diverging due to scatter in air as is shown in Figure 20.
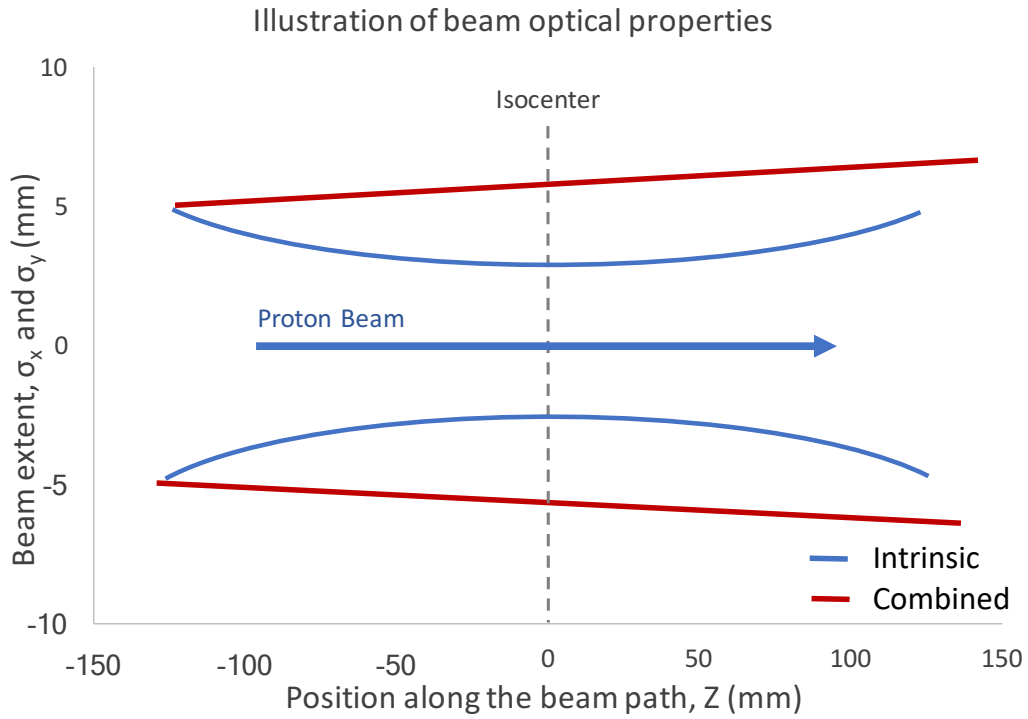
Figure 20. Illustrative display of spot size properties of the proton beam with the isocenter at Z position, 0 mm.

To calculate the intrinsic beam divergence at the nozzle exit, reference spot size measurements are taken at several positions around the isocenter, and Monte Carlo simulations with no divergence are created to account for air scatter. The slope of the change in measured spot sizes corresponds to the combined beam divergence from air and intrinsic properties [98], and the measured divergence, $\sigma_{div,measured}$, is assumed to be due to the combined effects defined as,

$$\sigma_{div,beam}^2 + \sigma_{div,air}^2 = \sigma_{div,measured}^2 \qquad (14)$$

where $\sigma_{div,beam}$ is the intrinsic beam divergence (in the *x*- and *y*- direction), and $\sigma_{div,air}$ is the beam divergence due to air scatter.

To derive, $\sigma_{div,measured}$, measurements around the isocenter are fit to the Gaussian function to acquire spot sizes, σ_x and σ_y. Beam divergences are then calculated from the slope of the change in spot size [98] and the divergence properties of the beam are defined independently as $\sigma_{div,x}$ and, $\sigma_{div,y}$. To derive $\sigma_{div,air}$, Monte Carlo simulation are created with an intrinsic beam divergence set to 0, and the change in beam size is assumed to be solely due to interactions in air.

The spatial and angular beam spread distributions are Gaussian [98] and correlated. This correlation is described by the emittance parameter responsible for the rotation of the phase space. As the beam at the nozzle exit was considered purely divergent, the beam emittance is set empirically [98],

$$\epsilon_u = 0.5 * \sigma_u * \pi \tag{15}$$

where ϵ_u is the beam emittance at the beam nozzle exit (in both the x and y-direction) that is calculated from the x- and y-spot sizes, σ_u, at the beam nozzle exit.

After the intrinsic beam properties are calculated, facility-specific Python modules are established. These modules estimate the beam divergence at the nozzle exit based on the nominal energy E_0. The beam divergence in the x-direction, $\sigma_{div,x}$ and in the y-direction, $\sigma_{div,y}$, are estimated by third-order polynomial approximation functions,

$$\sigma_{div,x}(E_0) = \sum_{1}^{n} a_i * E_0^i \tag{16}$$

and,
$$\sigma_{div,y}(E_0) = \sum_{1}^{n} b_i * E_0^i \tag{17}$$

2.4.6 Absolute dose matching

To describe the number of protons used to deliver the dose to the defined region, each individual delivered "spot" has an associated Monitoring Unit (MU), which is logged in the DICOM treatment plan. To simulate a treatment, it is therefore necessary to convert the number of prescribed MUs based on the measurements from a treatment facility. To do this type of absolute dose matching, there are different approaches that can be used based on the available data. For example, simulations can be compared to Faraday cup measurements of the number of protons that exited the nozzle [100], performing absolute dosimetry using a calorimeter [101], or using an ionization chamber for the reference dosimetry [102]. From these dosimetry techniques, only absolute dosimetry with a Faraday cup (FC) and reference dosimetry with an ionization chamber (IC) have been found suitable for routine clinical use and are considered to achieve good agreement between each other [103, 104].

Unfortunately, due to time constraints, for this work, neither measurement dose validation nor the recommended dose matching method was used. Instead, it was assumed that the treatment planning system was commissioned to deliver accurate dose to the prescribed region. The simulated physical dose due to protons was then used to normalize to the treatment planning prescribed dose. In this work, the dose is therefore reported as *mGy* or *mSv* per *Gy* received by the prescribed region as was simulated using TOPAS MC.

2.4.7   Patient-specific (TPS) parameters

Scripts were also written in Python to read and analyze the patient-specific

DICOM data log files. These files consist of header information and CT image, position

of organ structures that were contoured during treatment planning, and the ion beam plan

prepared by the treatment planning system optimized to avoid organs at risk. The data

about the patient and treatment setup is used to create inputs that are compatible with

TOPAS input parameter files. In addition, Python modules were created based on the

beam characterization methods described in the previous sections. These modules read

the DICOM ION treatment plan and convert the prescribed beam parameters, modifying

values based on the facility-specific conversion functions for Monte Carlo simulations.

This method was kept as general as possible, requiring only facility-specific conversion

functions to be changed to create the facility-specific parameter files.

2.4.8   Modeling the Maryland Proton Treatment Center proton beam

For this work, beam characterization modules were created from beam data

library (BDL) measurements made by medical physicists at the Maryland Proton

Treatment Center (MPTC) in Baltimore, MD. The integral depth dose (IDD) profiles and

spot measurements were performed for 19 energies ranging from 70 MeV to 245 MeV

as is shown in Figure 21. The IDD measurements had a range accuracy estimated to be

within 0.5 mm and the measured dose fluctuations within 1%. The same 19 energies are

simulated in TOPAS using a 10 cm by 10 cm field, with dose scored along the beam

path in a water phantom created from the GEANT4-preferred material for water,

G4_WATER.

To match the energy range, the simulation energy distribution was set to 0. After the simulation, the measured and simulated depth dose deposition curves are compared by evaluating peak-to-peak distances. The energy was incrementally changed until the difference was as close to 0 as possible. The physical range in the water phantom, *R90*, was then calculated for each Bragg peak as the distal 90% dose point for the 19 simulated and measured energies. For each matched energy range, the best energy spread was determined empirically by simulating different energy distributions around the estimated values. The best energy spread was again determined visually by evaluating and minimizing the point-to-point dose differences.

Measured depth dose deposition in water
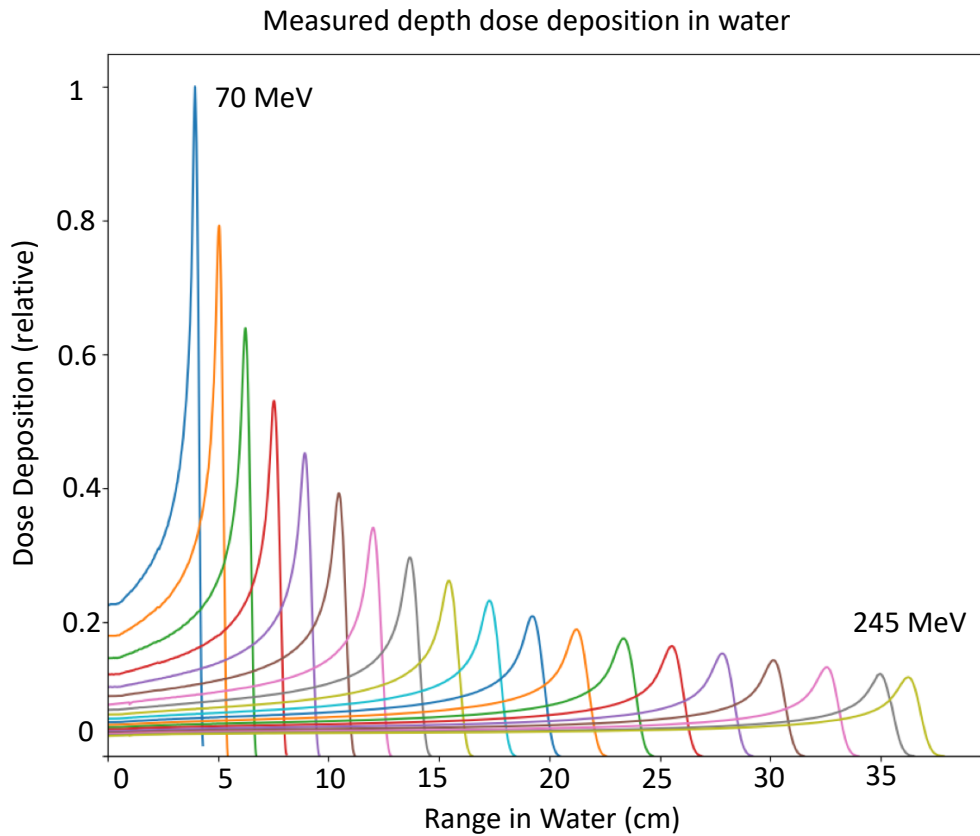
Figure 21. Measured integral of depth doses (IDDs) curves generated from 19 beam energies from the Maryland Proton Treatment Center. The first curve represents dose from the 70MeV beam and the last curve represents the 245 MeV beam.[†]

At the Maryland Proton Treatment Center, spot size measurements in the *x*- and *y*-lateral directions were taken at the isocenter, and several locations around it (at -20 cm, -10 cm, 0 cm, 10 cm, 20 cm from the isocenter). As is typically found at treatment facilities, these measurements are for the same energies as those used for range and distribution matching. The 2D distributions of spot size measurements at the isocenter

---

[†] Measurements obtained from Dr. Ulrich Langner at the Maryland Proton Treatment Center in Baltimore, MD.

are shown for all 19 beam energies in Figure 22 (A) and simulations of the spot sizes

around the isocenter are shown in Figure 22 (B). The measurements and simulations are

fitted automatically with an independent Gaussian function in each axis to accurately

and reproducibly extract the spot sizes in the *x*- and *y*- directions.

A) Measurements (isocenter)   B.1) TOPAS Simulation (+10 cm)
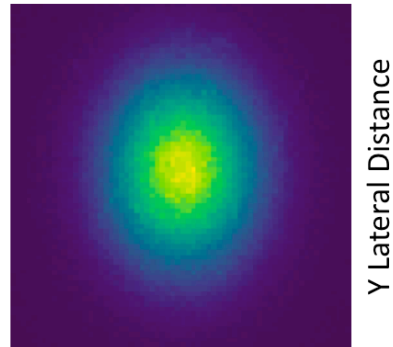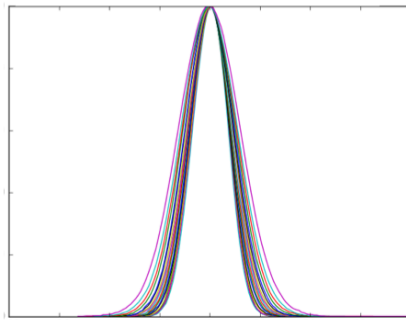
B.2) TOPAS Simulation (-10 cm)
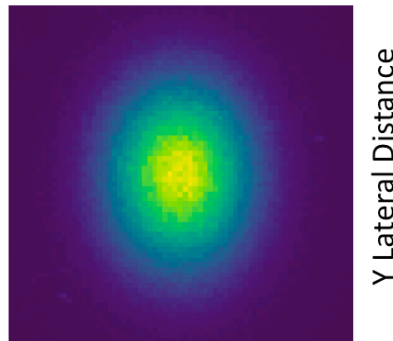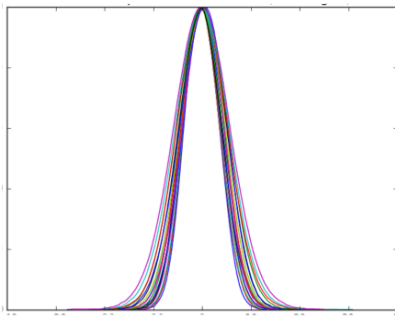
X Lateral Distance

Figure 22. Measured‡ and simulated spot sizes based on MPTC data with A) showing the measurements taken at isocenter and B.1) and B.2) showing the 2D profiles of the simulated spots at +10 cm and -10 cm from the isocenter.

‡ Measurements obtained from Dr. Ulrich Langner at the Maryland Proton Treatment Center in Baltimore, MD.

2.4.9 Patient specific (TPS) input data

TOPAS has the capability of reading DICOM CT image data and implement it directly into the Monte Carlo code to model patient anatomy [70]. This work focuses on converting the patient-specific treatment plans to simulate the proton beam used to irradiate the patient. DICOM ION plan files describe the treatment plan using one or multiple fields, with each field being described by a gantry angle and a collection of pencil beams. Each pencil beam is then characterized by its weight (MU), position in the isocenter plan, and its energy at the nozzle entrance. The *Patient Specific* module reads the DICOM ION plan description files converting that data to TOPAS input parameter files using the parameterized functions established from reference measurement data described in the previous sections.

2.4.10 Output-processing module

The TOPAS simulation code is relatively new and there have been some obstacles in its implementation. Several features of interest in previous TOPAS versions had issues or would increase computation time, therefore it was necessary to create post-processing modules to fill in those gaps. For example, to carry out organ dose calculation, it was necessary to create a post-processing module in Python. To do so, the *pydicom* Python library was used to import the patient DICOM CT image, DICOM RS structure set, and the output dose from TOPAS which in the DICOM RD format, which has the dose on the same grid as the DICOM CT. Using the DICOM RS data, a 3D binary mask is created for each organ structure. As each binary mask is of the same size

as the DICOM CT image and the dose grid, the two are overlaid to produce the organ-based dose, allowing for easy calculation of the organ mean dose. This is done for each particle-type, for both the dose and standard deviation. The dose during the TOPAS simulations is recorded on the same dose matrix as the DICOM CT image, split by particle type (proton, electron, neutron, and gammas) with the neutron dose split into energy bins and saved as separate dose files. For this study, to account for RBE, the dose from protons was corrected by a factor of 1.1 irrespective of energy [51] as is done by the treatment planning software. However, for more accurate calculation and further investigation of treatment planning software inaccuracies, an LET-corrected dose can be scored to take into account the varying RBE along the proton beam path.

Previously, ICRP 60 recommended a step function to parameterize energy-dependent neutron quality factors. More recently, ICRP 103 mad a change in this recommendation moving to a continuous energy dependence [105]. In this work, however, the neutron dose was scored by energy bins of 0 to 10 keV, 10 keV to 100 keV, 100 keV to 2 MeV, 2 MeV to 20 MeV, 20 MeV and above, to fit the previous (ICRP 60) radiation weighting factor model. However, the input parameter and output processing code can also be easily extended to have TOPAS score the neutron dose split by finer resolution energy bins to comply with the ICRP 103 continuous radiation weighting factors instead.

Using the organ-based dose, it is now possible to do further calculations. In the following section, risk calculations were completed for specific proton treatment

simulations using pediatric phantoms and realistic treatment plans, by applying post-processing risk calculation modules.

2.5 Applying beam model to calculate organ dose and calculate risk

ICRP reference computational phantoms of ages one and five [78] were sent to a certified medical physicist at the University of Maryland to add a common treatment plan. Medulloblastoma was chosen because it is one of the most common pediatric tumors of the central nervous system [106] and are commonly treated at MPTC. The phantoms are in DICOM CT image and DICOM RS structure format and were used to plan a treatment for a medulloblastoma-type tumor (Figure 23). Then, following the methods established in the previous sections, Monte Carlo simulations were run to determine the patient-specific, in- and out-of-field doses.
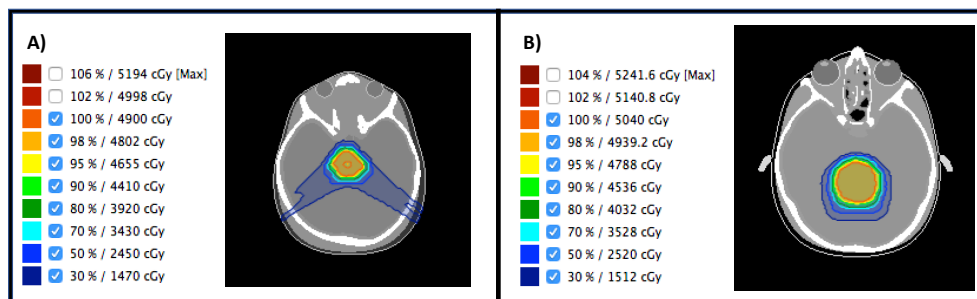
Figure 23. A) One- and B) Five- year old phantoms with a medulloblastoma-type treatment.

The dose to each voxel was scored during the TOPAS Monte Carlo simulations as a function of particle type. The output-processing modules were used to calculate

organ dose, taking into account the radiation weighting factors of all primary and secondary particles [107].

Modules were created in Python to use the patient equivalent organ dose calculated from the TOPAS Monte Carlo simulation of a proton therapy treatment, and implement the Biological Effects of Ionizing Radiation (BEIR) VII risk models [10], described in previous chapters. The modules calculate the BEIR VII Excess Relative Risk (ERR), Excess Absolute Risk (EAR), and the Lifetime Attributable Risks (LAR) for solid cancers of several organs. These models were applied to the doses received by the pediatric phantoms undergoing brain treatment simulations as described in the previous section.

The LAR is summed over an assumed age of 100 years of solid cancer incidence for the phantoms. On the recommendation of the BEIR VII report [10] the ERR is scaled on a log scale by a weight of 0.7 and the absolute risk is given a weight of 0.3. Of the large set of organs for which dose is calculated for each treatment, risk calculations of solid cancer incidence are only calculated for stomach, colon, liver, lung, and bladder cancers because of a lack of data and risk models for the other organs. Unexposed lifetime baseline risks based on Kocher et al. [25] and analyses of cancer incidence were based on cases diagnosed in the period 1958-1998 [108].

3   RESULTS

3.1   ANATOMY EXTENSIONS

For comparison purposes the mean organ doses for the chest and prostate cases were compared relative to that calculated for the heart and prostate, respectively. The resulting percent organ doses for the chest and the prostate irradiation cases are tabulated in percent dose differences for the reference and APE phantoms compared to the patient CAP CT are shown in Table 2 and 3 and are depicted in Figure 24.

Table 2. Examples of percent dose (%) in radiotherapy chest irradiations for the reference phantom, APE phantoms, and full CAP CT patient anatomies. The organs completely included in the partial-body CT images used to construct the APE are marked in bold.

Organ	Patient 1			Patient 2			Patient 3		
	Ref.	APE	Patient	Ref.	APE	Patient	Ref.	APE	Patient
Heart	88.569	100.14	100	88.569	100.14	100	88.569	100.14	100
Lung Left	22.845	28.774	28.714	22.845	28.774	28.714	22.845	28.774	28.714
Lung Right	22.274	19.725	19.711	22.274	19.725	19.711	22.274	19.725	19.711
Liver	4.268	11.653	12.504	4.268	11.653	12.504	4.268	11.653	12.504
Stomach	3.925	9.203	9.169	3.925	9.203	9.169	3.925	9.203	9.169
Bladder	0.032	0.032	0.045	0.032	0.032	0.045	0.032	0.032	0.045
Prostate	0.016	0.016	0.029	0.016	0.016	0.029	0.016	0.016	0.029

Table 3. Examples of percent dose (%) in radiotherapy prostate irradiations for the reference phantom, APE phantoms, and full CAP CT patient anatomies. The organs completely included in the partial-body CT images used to construct the APE are marked in bold.

Organ	*Patient 1*			*Patient 2*			*Patient 3*		
	Ref.	*APE*	*Patient*	*Ref.*	*APE*	*Patient*	*Ref.*	*APE*	*Patient*
Prostate	99.505	100.81	100	100.055	99.999	100	99.064	100.041	100
Bladder	45.877	87.911	87.898	46.13	65.529	65.516	45.674	95.419	95.439
Stomach	0.063	0.072	0.089	0.063	0.066	0.056	0.063	0.136	0.128
Liver	0.054	0.074	0.086	0.054	0.071	0.07	0.054	0.123	0.117
Heart	0.016	0.019	0.034	0.016	0.023	0.017	0.016	0.032	0.028
Lung Right	0.011	0.017	0.034	0.012	0.016	0.019	0.011	0.022	0.027
Lung Left	0.011	0.018	0.026	0.011	0.016	0.018	0.011	0.021	0.026

A. Chest Irradiation

B. Prostate Irradiation
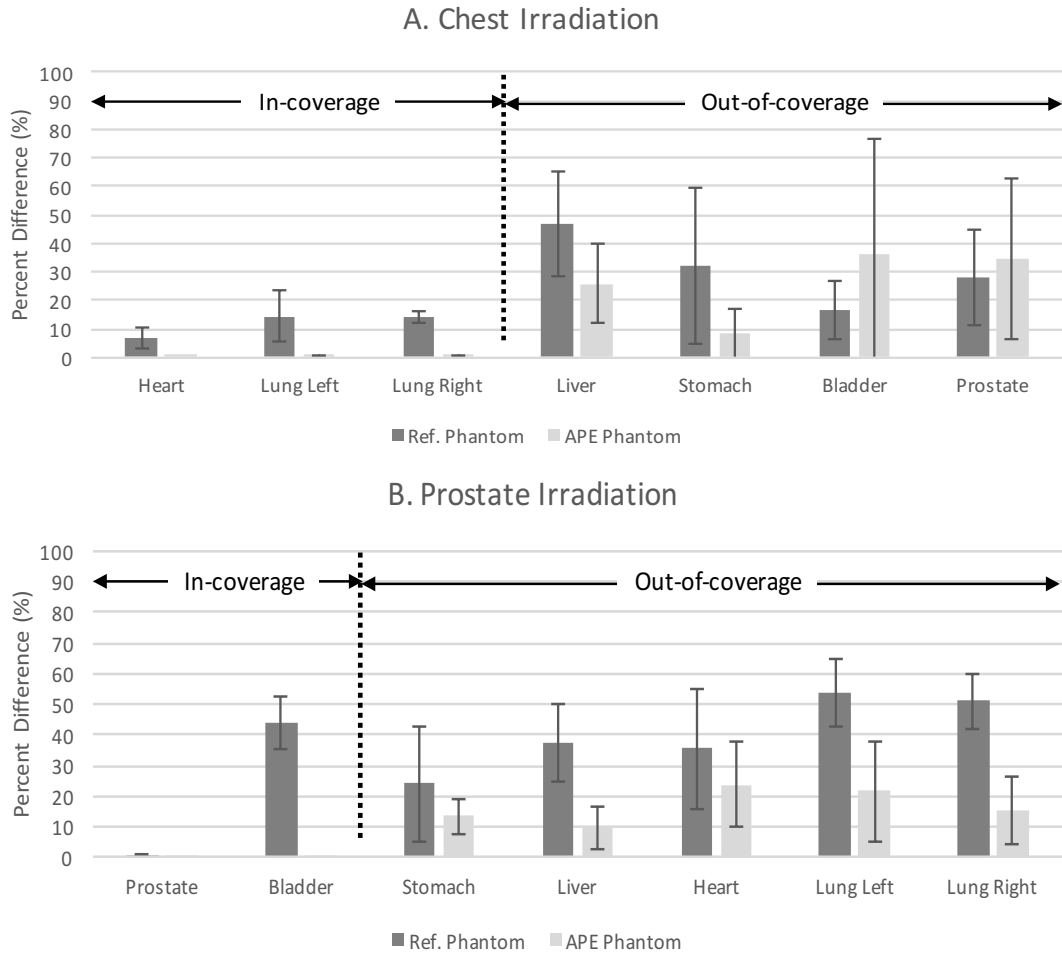
Figure 24. Absolute percent difference (%) for the reference and APE phantoms compared to that calculated using the full CAP CT scans averaged over the five patients for the (a) chest and (b) prostate irradiation cases. The organs located in-scan and out-of-scan.

These results show that the APE phantoms offer some dosimetric advantages compared to using reference phantoms. As expected, the APE phantoms and CAP CT images resulted in nearly identical dosimetry for those organs which are fully included in the partial-body CT used to construct the APE (e.g., heart and lungs for the chest irradiation case, and prostate and bladder for the prostate irradiation case). The reference

phantoms showed, on average, organ dose differences of up to 20% and 52% in the chest and prostate cases, respectively, compared to that calculated using the full CAP scan images. The improved accuracy in the dosimetry for the APE phantoms clearly demonstrates the benefit of using patient-specific anatomy.

The results for the out-of-scan organ dosimetry were mixed. In many cases the organ doses were improved compared to the reference phantom (e.g., difference of 57% for the reference phantom vs. 0.4% APE phantom for the stomach in patient 1 chest case). In other cases, however, there was no significant difference observed and sometimes the reference phantom showed better agreement (e.g. 6% reference phantom vs. 35% APE phantom for the heart in patient 2 abdomen case). Overall, however, the results still show that the APE phantoms perform similarly or better than the reference phantom. For the chest irradiation case, the average absolute difference for the out-of-scan organs was reduced from 31% (reference phantom) to 26% (APE phantom). For the prostate irradiation case, the average difference decreased from 41% (reference phantom) to 17% (APE phantom).

3.2 SCATTER COMPARISON

There was good agreement between MCNP6 and TOPAS simulations for scattering neutrons. However, there were significant discrepancies between the experimental setup and the simulations, which are not explained by sensitivity analysis. As an example, Figure 25 shows the physical bubbles produced by neutron interaction with the detector gel. The unfolded neutron energy spectrum from the bubble detectors results in large error bars, which don't overlap with the simulation results. The MCNP is a well-validated code [83, 84, 92, 109-113], and an AAPM Task Group 152, which was released after this work was completed, recommend the use of already established Monte Carlo simulation codes as the basis of out-of-field secondary neutron scatter validation studies [114].
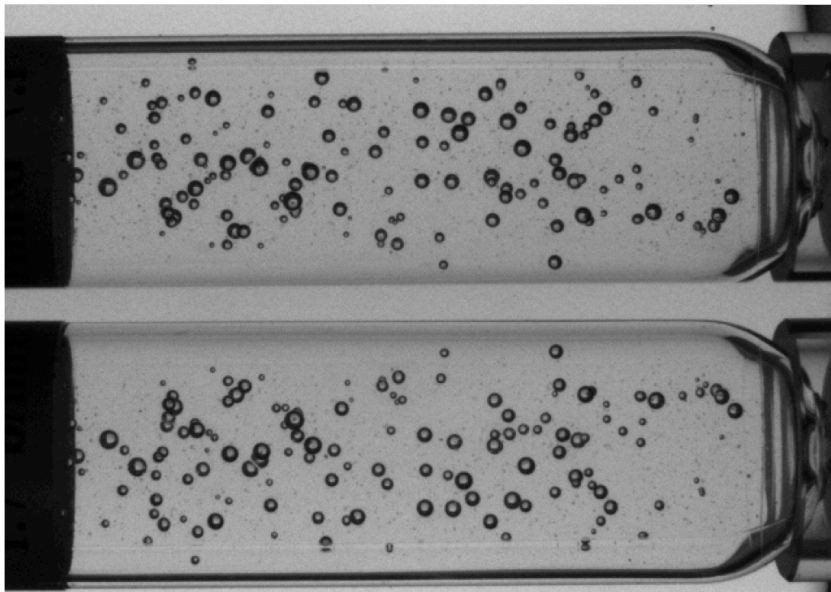
Figure 25. Photo of bubbles in detectors following irradiation by Cf-252.

A comparison of simulated and measured neutron spectra by TOPAS, MCNP, and Bubble Detectors in shown in Figure 26.

Comparison of measured and simulated neutron fluence
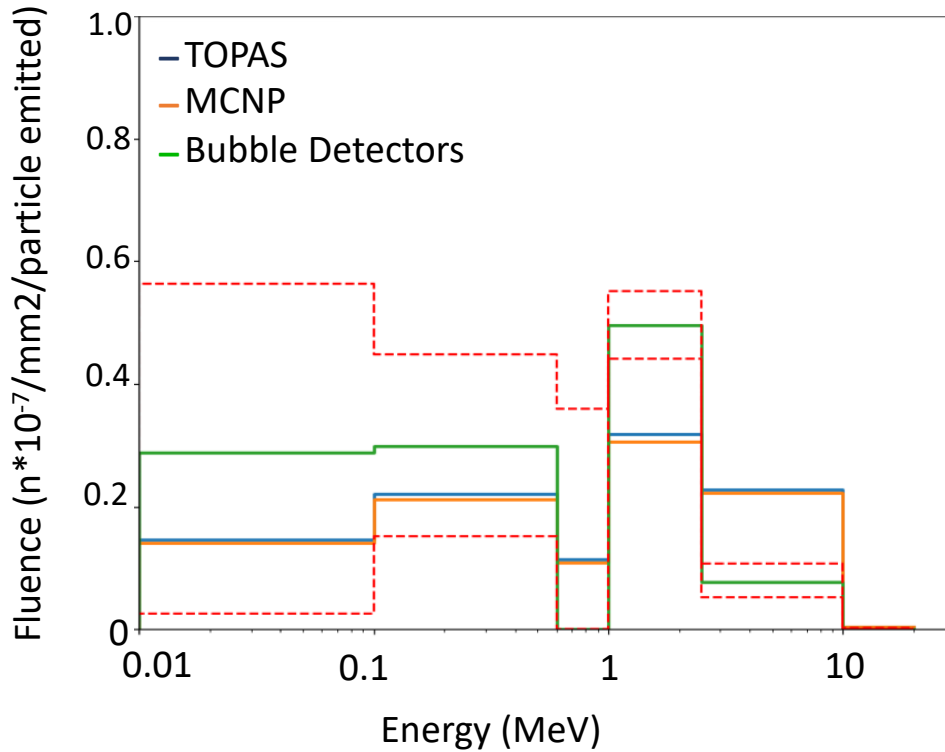
Figure 26. Comparison of simulated and measured spectrum by TOPAS, MCNP[4], and Bubble Detectors.

Further simulations were run using TOPAS to attempt to account for the discrepancies between theoretical and the unfolded response of bubble detectors; however, these simulations did not yield any significant differences, resulting in the

---

[4] MCNP simulations were carried out by Dr. Matthew Mille at the National Cancer Institute in Rockville, MD.

conclusion that the bubble detectors' sensitivity was not high enough to accommodate for such radiation levels. Therefore, it was determined that the best way to benchmark neutron scatter simulated by TOPAS is through comparisons with MCNP and evaluating neutron fluence using a finer resolution. The results are reported in Figure 27.
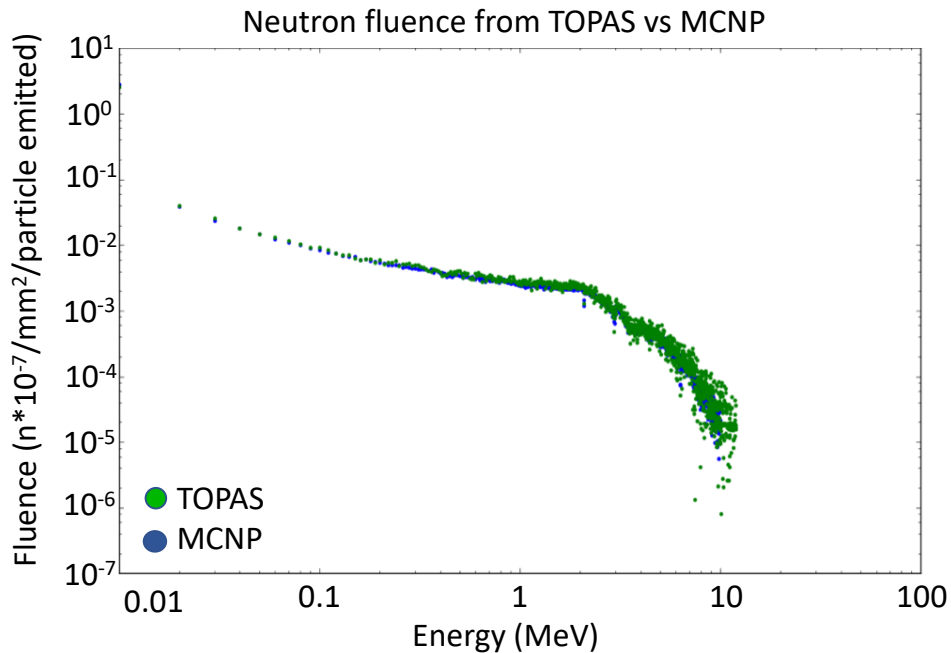
Figure 27. Comparison of simulated neutron spectrum by TOPAS and MCNP[5] in bins with finer resolution.

The fact that the simulations were well-matched leads to the conclusion that the bubble detectors were not be appropriate for experimental verification using this method, and that utilizing TOPAS simulations will result in comparable neutron fluence as that from the well-validate MCNP for the simulated regions.

---

[5] MCNP simulations were carried out by Dr. Matthew Mille at the National Cancer Institute in Rockville, MD.

3.3 PROTON BEAM MODELING

First, the simulated energy range and energy spread were matched with that measured at the Maryland Proton Treatment Center. To do so, the energy and energy spread were adjusted iteratively until the best match was achieved via visual inspection of the beam range and dose distribution, several of the curves are shown in Figure 28.
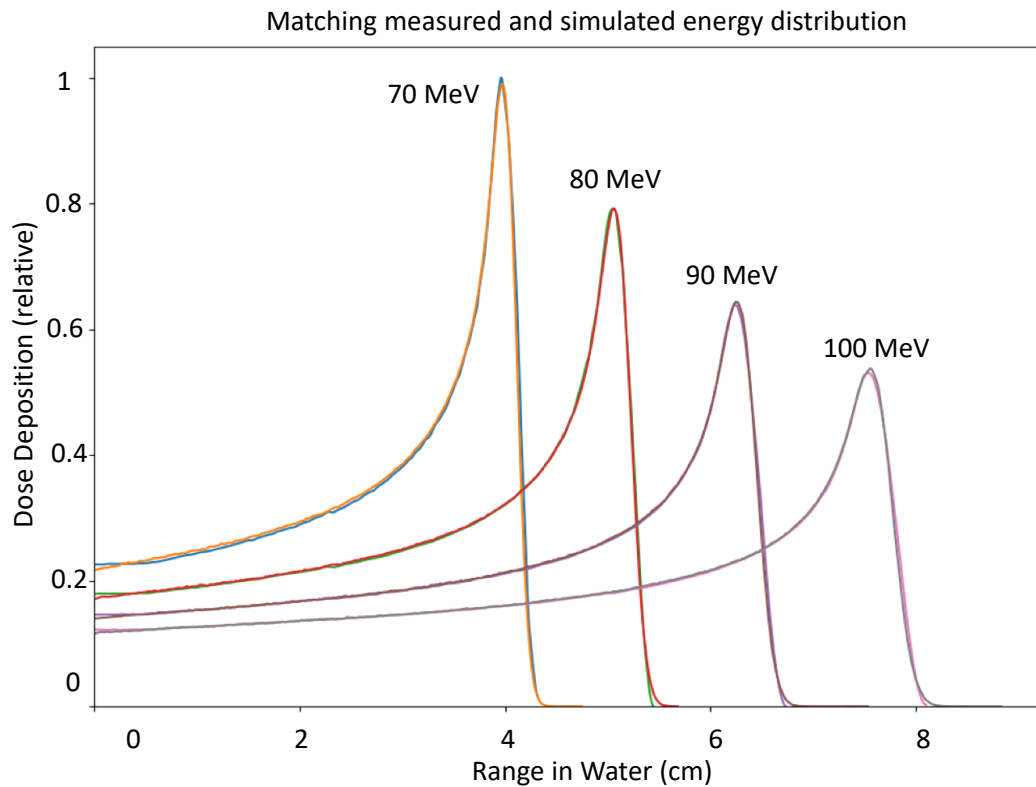
Figure 28. Sample of four (70, 80, 90, and 100 MeV) of the 19 depth-dose profiles of comparing measured dose deposition[6] and dose simulated by TOPAS.

---

[6] Measurements obtained from Dr. Ulrich Langner at the Maryland Proton Treatment Center in Baltimore, MD.

Figure 29 shows the calculated range correction linear fit calculated from the measurement and simulations.
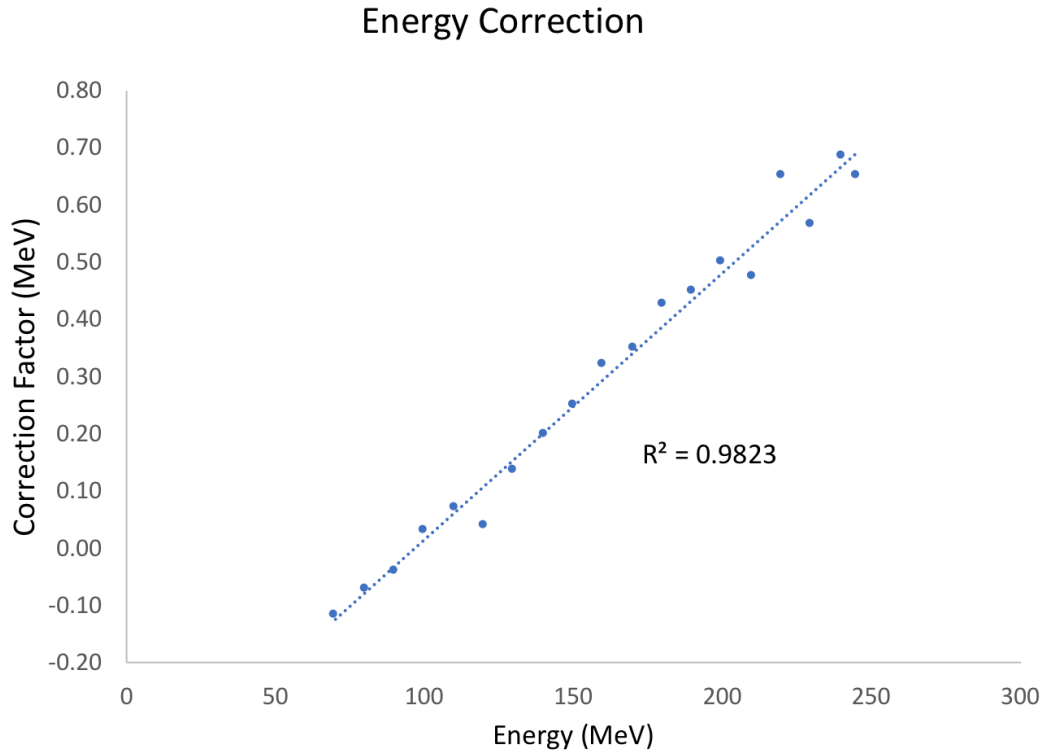
Energy Correction

Figure 29. Correcting for range differences by accounting for the energy difference between the beam nozzle entrance and the beam nozzle exit.

Once the simulations appropriately matched the measurement data for each of the 19 energies, energy standard deviation based on the prescribed nominal energy, E_0 from the third-order polynomial function as is shown in Figure 30. These functions are part of the MPTC facility-specific module that create TOPAS input parameters of the beam energy distribution.
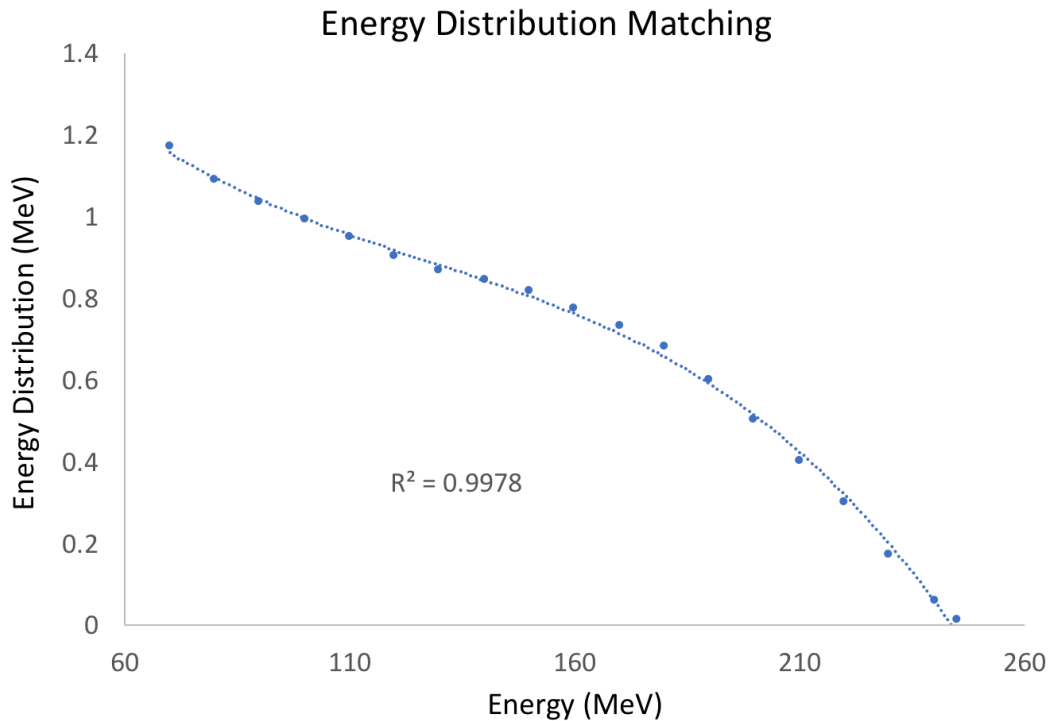
Figure 30. Energy distribution curve create based on the Maryland Proton Treatment Center.

3.3.1   Organ dose calculations

Using the Monte Carlo code TOPAS, proton treatments based on measurement data from the Maryland Proton Treatment Center were simulated using a one-year-old and a five-year-old computational phantom.

From this simulation study, it was noted that the majority of out-of-field dose is from secondary neutrons, as expected. Recent studies of neutron dose have shown organ equivalent doses decrease rapidly with increasing distance from the treatment volume [51]. Equivalent doses were analyzed for the phantoms and dose to organs for which structure contours were available were scored. To do so, dose from all particles, such as

neutron dose was scored per voxel in all possible organs and the equivalent organ dose

was combined per organ first as in Table 4 and Table 5, before combining them into

dose using the ICRP radiation weighting factors, shown in Table 5 and Table 6.

Table 4. Equivalent neutron dose (mSv/Gy) for the one-year-old phantom scored based on the energy step function matching the ICRP 60 weighting factors

Organ	*0-10 keV (mSv/Gy)*	*10 keV – 100 keV (mSv/Gy)*	*100 keV – 2 MeV (mSv/Gy)*	*2 MeV – 20 MeV (mSv/Gy)*	*Above 20 MeV (mSv/Gy)*
Adrenal Gland	0.00E+00	0.00E+00	0.00E+00	7.99E-05	4.18E-06
Bladder	0.00E+00	0.00E+00	0.00E+00	0.00E+00	1.90E-04
Brain	3.86E-05	5.25E-05	1.22E-04	1.23E-04	1.21E-04
Breast (adipose)	0.00E+00	0.00E+00	0.00E+00	0.00E+00	0.00E+00
Bronchus	0.00E+00	0.00E+00	3.09E-05	1.05E-04	2.33E-04
Colon	0.00E+00	2.58E-06	3.03E-05	1.03E-04	1.23E-04
Ear (external)	0.00E+00	6.36E-05	1.38E-04	1.32E-04	7.62E-05
Esophagus	0.00E+00	1.33E-06	1.27E-04	8.71E-05	2.03E-04
Eyes	2.80E-08	2.53E-05	1.73E-04	1.35E-04	1.08E-04
Gallbladder	0.00E+00	0.00E+00	2.47E-05	1.13E-04	9.48E-06
Heart	0.00E+00	1.49E-05	7.98E-05	1.04E-04	1.18E-04
Kidney	0.00E+00	0.00E+00	4.40E-05	1.14E-04	6.25E-05
Larynx	0.00E+00	5.91E-08	9.40E-05	1.05E-04	1.05E-04
Lens	0.00E+00	0.00E+00	0.00E+00	0.00E+00	0.00E+00
Liver	0.00E+00	0.00E+00	1.02E-04	1.04E-04	1.25E-04
Lung	8.01E-06	1.09E-08	1.80E-04	2.29E-04	2.36E-04
Nose	0.00E+00	0.00E+00	1.52E-04	7.95E-05	1.65E-04
Pancreas	0.00E+00	0.00E+00	4.63E-06	5.54E-05	9.40E-05
Parotids	6.73E-08	5.85E-05	1.19E-04	1.18E-04	1.05E-04

Table 4. (Cont.)

Organ	0-10 keV (mSv/Gy)	10 keV – 100 keV (mSv/Gy)	100 keV – 2 MeV (mSv/Gy)	2 MeV – 20 MeV (mSv/Gy)	Above 20 MeV (mSv/Gy)
Penis	0.00E+00	0.00E+00	0.00E+00	0.00E+00	4.51E-05
Pituitary	0.00E+00	5.56E-05	5.14E-05	1.13E-04	6.86E-05
Prostate	0.00E+00	0.00E+00	0.00E+00	1.31E-04	0.00E+00
Scrotum	0.00E+00	0.00E+00	0.00E+00	0.00E+00	0.00E+00
Skin	3.59E-05	4.68E-05	1.17E-04	1.19E-04	1.20E-04
Spleen	0.00E+00	0.00E+00	1.19E-04	1.24E-04	6.94E-05
Stomach	0.00E+00	5.40E-09	5.67E-05	1.04E-04	7.43E-05
Subl gland	0.00E+00	3.89E-07	7.31E-05	1.15E-04	1.36E-04
Submand gland	0.00E+00	5.06E-06	9.52E-05	1.13E-04	8.39E-05
Thymus	0.00E+00	1.24E-07	9.18E-05	1.07E-04	1.20E-04
Thyroid	0.00E+00	0.00E+00	8.92E-05	1.14E-04	1.37E-04
Tongue	5.60E-09	5.92E-06	9.21E-05	1.12E-04	1.53E-04
Tonsil	0.00E+00	1.94E-06	1.12E-04	1.55E-04	6.13E-05
Trachea	0.00E+00	0.00E+00	1.66E-05	9.26E-05	1.34E-04

Table 5. Neutron equivalent dose (mSy/Gy) for the five-year-old phantom scored based on the energy step function to match the ICRP 60 weighting factors

Organ	*0-10 keV (mSv/Gy)*	*10 keV – 100 keV (mSv/Gy)*	*100 keV – 2 MeV (mSv/Gy)*	*2 MeV – 20 MeV (mSv/Gy)*	*Above 20 MeV (mSv/Gy)*
Adrenal Gland	0.00E+00	0.00E+00	2.67E-05	1.51E-04	5.84E-05
Bladder	0.00E+00	0.00E+00	0.00E+00	2.70E-04	3.71E-05
Brain	4.72E-05	8.47E-05	1.83E-04	2.06E-04	1.75E-04
Breast (adipose)	0.00E+00	0.00E+00	0.00E+00	0.00E+00	0.00E+00
Bronchus	0.00E+00	0.00E+00	2.23E-04	1.78E-04	1.50E-04
Colon	0.00E+00	0.00E+00	6.98E-06	1.91E-04	1.74E-04
Ear (external)	9.34E-09	4.98E-05	2.09E-04	1.93E-04	1.18E-04
Esophagus	0.00E+00	0.00E+00	2.13E-04	1.74E-04	1.38E-04
Eyes	0.00E+00	9.38E-05	1.61E-04	1.96E-04	1.81E-04
Gallbladder	0.00E+00	0.00E+00	0.00E+00	1.28E-04	1.66E-04
Heart	0.00E+00	5.28E-07	1.42E-04	1.66E-04	1.36E-04
Kidney	0.00E+00	0.00E+00	8.85E-05	1.92E-04	1.17E-04
Larynx	5.46E-09	2.13E-04	1.07E-04	1.69E-04	2.00E-04
Lens	0.00E+00	0.00E+00	1.99E-04	1.32E-05	2.97E-04
Liver	0.00E+00	2.19E-05	1.33E-04	1.68E-04	1.70E-04
Lung	0.00E+00	4.23E-05	3.07E-04	3.66E-04	3.13E-04
Nose	0.00E+00	0.00E+00	6.54E-05	1.27E-04	4.08E-05
Pancreas	0.00E+00	0.00E+00	0.00E+00	1.57E-04	1.56E-04
Parotids	5.46E-09	7.05E-05	1.50E-04	1.82E-04	1.81E-04
Penis	0.00E+00	0.00E+00	0.00E+00	0.00E+00	0.00E+00
Pituitary	0.00E+00	0.00E+00	5.38E-05	2.30E-04	5.56E-05
Prostate	0.00E+00	0.00E+00	0.00E+00	0.00E+00	0.00E+00
Scrotum	0.00E+00	0.00E+00	0.00E+00	0.00E+00	0.00E+00
Skin	4.42E-05	7.80E-05	1.75E-04	1.96E-04	1.74E-04

Table 5. (Cont.)

Organ	0-10 keV (mSv/Gy)	10 keV – 100 keV (mSv/Gy)	100 keV – 2 MeV (mSv/Gy)	2 MeV – 20 MeV (mSv/Gy)	Above 20 MeV (mSv/Gy)
Spleen	0.00E+00	8.42E-08	2.17E-04	1.68E-04	2.13E-04
Stomach	0.00E+00	1.11E-08	1.56E-04	1.70E-04	2.09E-04
Subl gland	0.00E+00	0.00E+00	1.22E-04	1.90E-04	1.31E-04
Submand gland	2.02E-07	4.44E-05	1.69E-04	1.75E-04	1.75E-04
Thymus	0.00E+00	1.26E-06	1.85E-04	1.80E-04	1.59E-04
Thyroid	0.00E+00	0.00E+00	1.14E-04	1.73E-04	1.69E-04
Tongue	1.07E-04	8.97E-05	1.38E-04	1.73E-04	1.35E-04
Tonsil	0.00E+00	2.02E-04	1.34E-04	1.79E-04	1.91E-04
Trachea	0.00E+00	0.00E+00	9.21E-05	1.99E-04	1.79E-04

Table 6. TOPAS organ dose calculated of the medulloblastoma 3 field scanning beam proton treatment for the 1-year-old-phantom

Organ	*Total Dose (mSv/Gy)*	*Neutron Dose* (mSv/Gy)*	*Dose P (mSv/Gy)*	*SD P (mSv/Gy)*	*Dose E (mSv/Gy)*	*SD E (mSv/Gy)*	*Dose G (mSv/Gy)*	*SD G (mSv/Gy)*
Adrenal Gland	8.20E-04	8.20E-04	0.00E+00	1.42E-08	0.00E+00	7.95E-09	1.44E-07	1.94E-11
Bladder	9.50E-04	9.50E-04	0.00E+00	2.55E-08	0.00E+00	8.23E-09	9.30E-08	1.92E-11
Brain	1.82E+02	5.00E-03	1.76E+02	6.27E-05	6.04E+00	1.38E-06	1.43E-05	1.33E-10
Breast (adipose)	0.00E+00	0.00E+00	0.00E+00	4.44E-08	0.00E+00	1.00E-08	0.00E+00	0.00E+00
Bronchus	4.26E-03	2.84E-03	0.00E+00	7.28E-08	1.42E-03	1.38E-08	1.39E-07	1.80E-11
Colon	2.28E-03	2.28E-03	0.00E+00	1.45E-07	0.00E+00	8.10E-09	1.69E-07	2.11E-11
Ear (external)	1.25E-01	5.09E-03	1.14E-01	3.22E-07	5.80E-03	2.39E-08	8.16E-07	6.68E-11
Esophagus	4.44E-03	4.43E-03	0.00E+00	7.37E-08	0.00E+00	8.61E-09	2.46E-07	2.21E-11
Eyes	5.61E-03	5.61E-03	0.00E+00	9.44E-08	0.00E+00	8.31E-09	2.03E-07	2.34E-11
Gallbladder	1.67E-03	1.67E-03	0.00E+00	6.33E-08	0.00E+00	8.01E-09	1.20E-07	2.54E-11
Heart	3.38E-03	3.38E-03	0.00E+00	8.69E-08	0.00E+00	8.13E-09	1.80E-07	2.45E-11
Kidney	2.33E-03	2.33E-03	0.00E+00	9.22E-08	0.00E+00	8.21E-09	1.62E-07	2.05E-11
Larynx	5.35E-03	3.46E-03	0.00E+00	9.48E-08	1.89E-03	1.05E-08	1.88E-07	2.24E-11
Lens	9.42E-08	0.00E+00	0.00E+00	4.93E-09	0.00E+00	5.92E-09	9.42E-08	1.23E-11
Liver	3.69E-03	3.69E-03	0.00E+00	9.01E-08	0.00E+00	8.01E-09	1.63E-07	2.16E-11
Lung	7.58E-03	7.10E-03	0.00E+00	1.36E-07	4.72E-04	9.05E-09	3.44E-07	3.51E-11

*Neutron dose is the organ dose weighted based on the ICRP 60 radiation weighting factors with the neutron dose data.

Table 6. (Cont.)

Organ	*Total Dose (mSv/Gy)*	*Neutron Dose* (mSv/Gy)*	*Dose P (mSv/Gy)*	*SD P (mSv/Gy)*	*Dose E (mSv/Gy)*	*SD E (mSv/Gy)*	*Dose G (mSv/Gy)*	*SD G (mSv/Gy)*
Pancreas	1.12E-03	1.12E-03	0.00E+00	5.20E-08	0.00E+00	8.47E-09	1.09E-07	1.92E-11
Parotids	3.72E-02	4.68E-03	3.06E-02	1.39E-07	1.89E-03	1.12E-08	2.38E-07	2.25E-11
Penis	2.26E-04	2.26E-04	0.00E+00	4.93E-09	0.00E+00	1.11E-08	1.46E-07	1.58E-11
Pituitary	5.55E+01	3.06E-03	5.55E+01	8.88E-05	2.28E-02	1.08E-07	5.16E-07	3.07E-11
Prostate	1.31E-03	1.31E-03	0.00E+00	0.00E+00	0.00E+00	1.37E-09	0.00E+00	0.00E+00
Scrotum	1.22E-07	0.00E+00	0.00E+00	1.38E-07	0.00E+00	8.92E-09	1.22E-07	1.42E-11
Skin	1.50E+02	4.78E-03	1.45E+02	4.20E-05	5.58E+00	7.24E-07	1.43E-05	1.28E-10
Spleen	3.97E-03	3.97E-03	0.00E+00	1.15E-07	0.00E+00	8.01E-09	1.33E-07	1.96E-11
Stomach	2.55E-03	2.55E-03	0.00E+00	1.13E-07	0.00E+00	7.93E-09	1.52E-07	2.06E-11
Sublingual gland	3.30E-03	3.30E-03	0.00E+00	1.01E-07	0.00E+00	8.62E-09	2.23E-07	2.09E-11
Submand. gland	4.45E-03	3.51E-03	0.00E+00	8.71E-08	9.43E-04	8.79E-09	1.76E-07	2.02E-11
Thymus	3.51E-03	3.51E-03	0.00E+00	1.02E-07	0.00E+00	8.60E-09	1.77E-07	2.12E-11
Thyroid	3.61E-03	3.60E-03	0.00E+00	8.45E-08	0.00E+00	8.86E-09	1.25E-07	1.72E-11
Tongue	5.67E-03	3.78E-03	0.00E+00	9.54E-08	1.89E-03	9.63E-09	2.08E-07	2.31E-11
Tonsil	5.07E-03	4.12E-03	0.00E+00	1.51E-07	9.47E-04	1.04E-08	1.45E-07	1.83E-11
Trachea	1.93E-03	1.93E-03	0.00E+00	6.46E-08	0.00E+00	8.12E-09	1.66E-07	1.93E-11

Table 7. TOPAS organ dose calculated of the medulloblastoma 3 field scanning beam proton treatment for the five-year-old treatment

Organ	Total Dose (mSv/Gy)	Neutron Dose* (mSv/Gy)	Dose P (mSv/Gy)	SD P (mSv/Gy)	Dose E (mSv/Gy)	SD E (mSv/Gy)	Dose G (mSv/Gy)	SD G (mSv/Gy)
Adrenal Gland	2.33E-03	2.33E-03	0.00E+00	7.65E-08	0.00E+00	6.49E-09	1.59E-07	5.11E-11
Bladder	2.88E-03	2.88E-03	0.00E+00	9.49E-08	0.00E+00	6.60E-09	1.55E-07	2.04E-11
Brain	2.59E+02	7.68E-03	2.52E+02	9.08E-05	6.92E+00	1.64E-06	1.70E-05	1.08E-10
Breast (adipose)	7.07E-08	0.00E+00	0.00E+00	0.00E+00	0.00E+00	5.20E-09	7.07E-08	1.01E-11
Bronchus	7.00E-03	7.00E-03	0.00E+00	8.32E-08	0.00E+00	7.12E-09	1.53E-07	1.71E-11
Colon	2.92E-03	2.92E-03	0.00E+00	9.08E-08	0.00E+00	6.52E-09	1.47E-07	2.50E-11
Ear (external)	2.77E+00	7.21E-03	2.62E+00	3.04E-06	1.48E-01	1.62E-07	1.48E-06	6.59E-11
Esophagus	6.69E-03	6.69E-03	0.00E+00	6.14E-08	0.00E+00	7.76E-09	1.43E-07	2.47E-11
Eyes	7.01E-03	7.01E-03	0.00E+00	8.01E-08	0.00E+00	7.40E-09	1.79E-07	2.41E-11
Gallbladder	2.12E-03	2.12E-03	0.00E+00	8.71E-08	0.00E+00	6.79E-09	1.20E-07	1.19E-11
Heart	5.19E-03	5.19E-03	0.00E+00	7.73E-08	0.00E+00	6.68E-09	1.45E-07	2.45E-11
Kidney	4.27E-03	4.27E-03	0.00E+00	7.74E-08	0.00E+00	6.67E-09	1.47E-07	2.24E-11
Larynx	1.02E-02	6.96E-03	0.00E+00	7.50E-08	3.24E-03	9.53E-09	1.64E-07	2.48E-11
Lens	5.60E-03	5.60E-03	0.00E+00	6.17E-08	0.00E+00	8.29E-09	1.06E-07	2.36E-11
Liver	5.41E-03	5.41E-03	0.00E+00	7.60E-08	0.00E+00	6.49E-09	1.46E-07	2.53E-11

*Neutron dose is the organ dose weighted based on the ICRP 60 radiation weighting factors with the neutron dose data

Table 7. (Cont.)

Organ	Total Dose (mSv/Gy)	Neutron Dose* (mSv/Gy)	Dose P (mSv/Gy)	SD P (mSv/Gy)	Dose E (mSv/Gy)	SD E (mSv/Gy)	Dose G (mSv/Gy)	SD G (mSv/Gy)
Lung	1.23E-02	1.18E-02	0.00E+00	1.05E-07	5.00E-04	7.75E-09	3.37E-07	4.86E-11
Nose	3.83E-03	2.79E-03	0.00E+00	8.67E-08	1.05E-03	6.44E-09	2.93E-07	2.96E-11
Pancreas	2.35E-03	2.35E-03	0.00E+00	8.40E-08	0.00E+00	6.52E-09	1.32E-07	2.22E-11
Parotids	3.26E-02	6.43E-03	2.41E-02	8.28E-08	2.08E-03	1.08E-08	2.17E-07	2.58E-11
Penis	9.66E-08	0.00E+00	0.00E+00	7.57E-09	0.00E+00	6.07E-09	9.66E-08	1.18E-11
Pituitary	4.70E-03	3.66E-03	0.00E+00	7.49E-08	1.05E-03	1.27E-08	2.65E-07	2.68E-11
Scrotum	0.00E+00	0.00E+00	0.00E+00	9.46E-08	0.00E+00	6.21E-09	0.00E+00	0.00E+00
Skin	2.05E+02	7.33E-03	1.99E+02	5.19E-05	6.44E+00	7.38E-07	1.79E-05	1.02E-10
Spleen	7.09E-03	7.09E-03	0.00E+00	8.78E-08	0.00E+00	6.63E-09	1.52E-07	2.48E-11
Stomach	5.86E-03	5.86E-03	0.00E+00	7.87E-08	0.00E+00	6.59E-09	1.36E-07	2.18E-11
Subl gland	4.99E-03	4.99E-03	0.00E+00	8.42E-08	0.00E+00	7.63E-09	1.78E-07	2.57E-11
Submand gland	7.44E-03	6.44E-03	0.00E+00	8.25E-08	9.99E-04	9.50E-09	2.23E-07	2.90E-11
Thymus	6.30E-03	6.30E-03	0.00E+00	7.73E-08	0.00E+00	7.09E-09	1.43E-07	2.77E-11
Thyroid	4.86E-03	4.86E-03	0.00E+00	7.10E-08	0.00E+00	7.73E-09	1.38E-07	2.93E-11
Tongue	8.64E-03	6.60E-03	0.00E+00	7.93E-08	2.05E-03	9.13E-09	2.10E-07	2.52E-11
Tonsil	2.16E-02	7.44E-03	1.21E-02	9.32E-08	2.05E-03	1.23E-08	2.62E-07	2.47E-11
Trachea	4.73E-03	4.73E-03	0.00E+00	8.54E-08	0.00E+00	7.27E-09	1.32E-07	3.32E-11

3.4 RISK CALCULATIONS OF SECONDARY CANCER INCIDENCE

Excess Relative Risks (ERR), Excess Absolute Risks (EAR) and Lifetime Attributable (LAR) risks of cancer incidence due to the proton therapy were calculated for the one and five-year-old phantoms. While the data for cancer-incidence in general is numerous, data is limited for organ-specific cancer incidence limiting the risk analysis possible. As such, ERR's was calculated for both cases for stomach, colon, liver, lung, and bladder. EAR's was calculated for both cases for stomach, colon, liver, lung, bladder and prostate. ERR and EAR calculated for the one-year-old phantom are shown below.
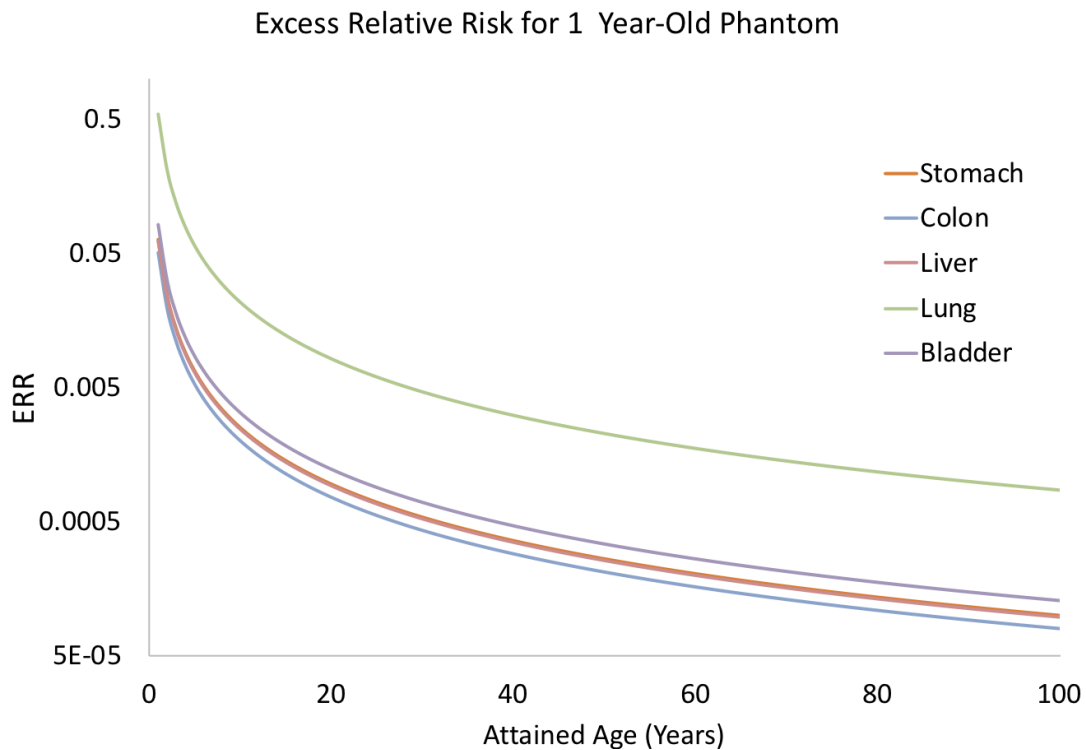
Figure 31. ERRs calculated for a scanning proton therapy medulloblastoma treatment of a 1-year-old phantom

91

Excess Absolute Risk for 1-Year-Old Phantom
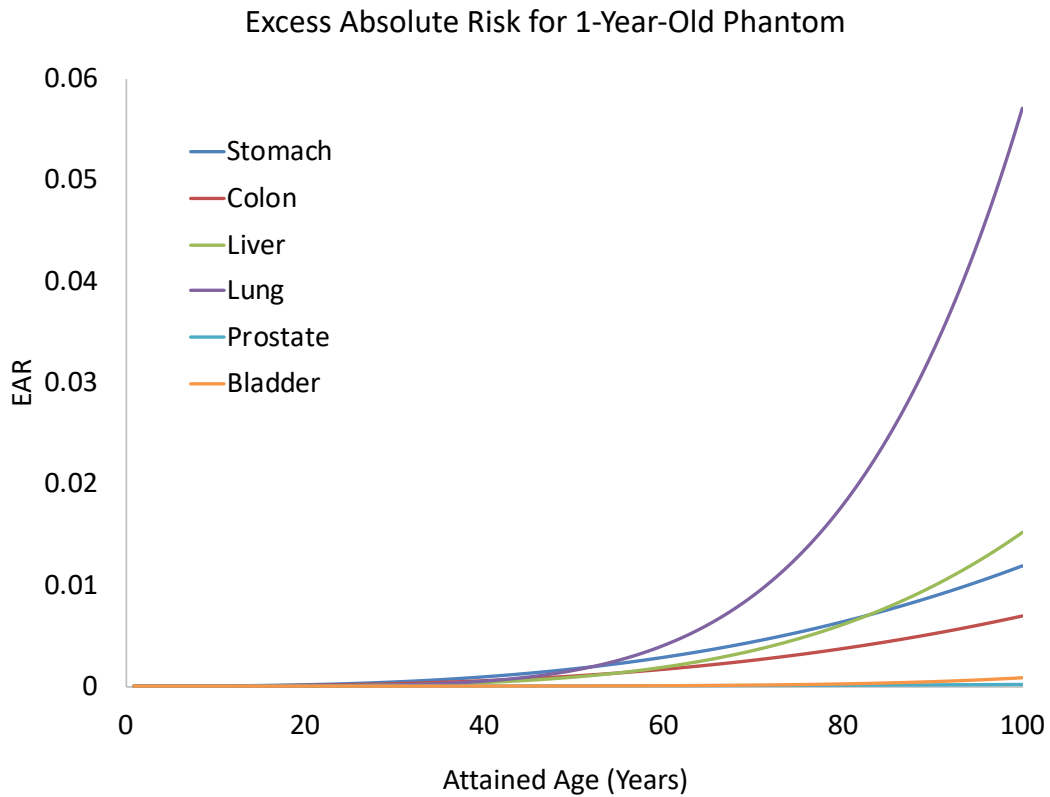
Figure 32. EAR calculations for a proton therapy medulloblastoma treatment of a 1-year-old phantom

LAR's were calculated for the one-year-old, and five-year-old phantoms for cancer tumor induction in the stomach, colon, liver, lung, and bladder shown in calculated by the BEIR VII risk models using the linear dose-response models, shown in Table 7 below.

Table 8. Table of Lifetime Attributable Risk of cancer incidence due do the proton therapy treatment of the one and five-year-old phantoms

Organ	*One-year-old phantom*	*Five-year-old phantom*
	LAR (%)	*LAR (%)*
Stomach	0.00244	0.00339
Colon	0.00623	0.00483
Liver	0.00135	0.00119
Lung	0.111	0.108
Bladder	0.00371	0.00678

4   DISCUSSION

4.1   OVERVIEW

The goal of this dissertation was to investigate and develop methods that improve dose reconstruction in epidemiologic studies. This work will be utilized by epidemiologists for further investigation of the radiation dose-response model. It will also allow for dose reconstruction of patients undergoing proton therapy with potentially higher accuracy than that estimated by clinicians administering the dose. In addition, these methods can be used to calculate the risks from the low doses received using already established risk models.

4.2 ANATOMY EXTENSION

The main objective of the anatomy extension section was to develop an improved method for dose reconstruction of patients undergoing radiotherapy using the limited available anatomical data. One important application is for epidemiologic studies aimed at assessing the risks of late-effects following both photon and proton radiotherapy. For example, at the National Cancer Institute it was found that the thyroid is consistently located just beyond the typical CT scan range used for breast radiotherapy planning. And while the majority of second primary tumors occur within the beam-bordering region, previous studies have found that about 20% are located in tissues 5 to 30 cm away from the irradiated volume [75]. Therefore, methods are needed to accurately estimate the dose deposited in these regions of epidemiologic interest.

To account for the fact that this region is not of clinical interest and there is no anatomy representing organs and tissue in these regions, our anatomy extension algorithm helps aid in the assessment of dose simultaneous near and distant to the tissues of primary clinical interest. It is worthwhile to note that in this study, the organ doses were compared between a reference phantom and patient chest-abdominal-pelvic (CAP) CT scans and then between the APE phantoms and patient CAP CT scans. Organ doses between body size-matched phantoms and patient CAP CT scans were also compared. However, this latter comparison was not included in this dissertation because there was not an observably clear improvement compared to simply using reference phantoms. It was found that anatomical variability in different patients cannot be captured simply by changing the size of the phantoms, which underscores the importance of the APE

technique. This is done by capturing as much patient-specific anatomy as possible for improving the dosimetry. While not perfect, the APE method has some important advantages over previous dose reconstruction methods that do not consider patient-specific anatomy at all [8, 13, 71].

The author acknowledges the limitations of the APE method as follows. First, manual contouring of patient CT images is still required. However, the phantom CT images are already contoured and do not require further modification. It was presumed that key organs at risk are already segmented during radiotherapy planning and no further contouring would be required for this work. Atlas-based automatic segmentation methods are currently being explored for additional organs of interest in epidemiologic studies and it may be possible to incorporate this into this APE method. Second, the author has so far only demonstrated the APE using images extracted from CAP scans (i.e. from lung apices to symphysis pubis). The performance of the APE phantoms generated using other types of CT scans (e.g. Head and Neck CT scans) has not been tested, though it is believed the APE method is applicable to the entire body. Third, although the APE phantoms provide more accurate organ dose estimation than the reference phantom, the author acknowledges that a dose discrepancy between APE phantoms and patients still exists and methods are currently being investigated to resolve such issues.

4.3 TREATMENT SIMULATIONS

4.3.1 TOPAS benchmarking

The original goal was to use bubble detectors to benchmark neutrons scatter, due to their promising features of good spatial resolution and ability to provide a neutron energy spectrum. In this work, a comparison study of neutron scatter was created looking at neutron fluence due to a Cf-252 source and scatter through a phantom. However, to achieve good statistical power, it required a lengthy time of irradiation. One of the energy bins (above 10 MeV) only received one bubble detector after an irradiation of over 70 hours. Therefore, for this study it was more practical to use an already-established Monte Carlo code, MCNP [92].

In addition, an AAPM Task Group Report No. 158 *Measurement and calculation of doses outside the treated volume from external-beam radiation therapy* [114] was released after this work was completed. This task group report suggests methods of calculating neutron dose measurements at clinical facilities investigating neutron dose from their system. It recommends not using bubble detectors for neutron dose validation from proton therapy treatments.

As such, while the measurements in this work were of neutrons in the range that were acceptable for use of bubble detectors, ultimately comparisons with MCNP were used. The two simulation codes compared well in the regions below 20 MeV. However, it will be beneficial to test the TOPAS code using a higher-energy source (above 20 MeV). In addition, a higher dose rate or less shielding would be recommended for further comparison between TOPAS simulations and bubble detector measurements.

Additionally, further comparisons of scattered of neutron energies in the 20-275 MeV would also be recommended using other Monte Carlo codes.

While this study used methods based on the TOPAS MC code, other methods should also be considered for epidemiologic studies. For example, there have been recent developments in analytical methods for neutron dose calculation for large-scale epidemiologic studies, such as the methods used by Zhang et al. [115] and Anferov, et al [116]. Dose comparisons between these analytical methods and Monte Carlo methods using TOPAS would be suggested for further investigations. Additionally, further studies can be created to investigate dose differences due to the uncertainties produced by the conversions of CT image (measured in HU units) to material composition [117, 118].

4.3.2   Facility-specific simulation

In this work, a method is described to determine the physical properties of the proton delivery system, which is based on a set of easily-available reference measurements used during the commissioning of the treatment planning system. The benefit of this method is that 1) these are standard measurements taken at proton therapy centers, and 2) this method does not require simulating the entire treatment head, so it does not require blueprints or more extensive measurement data, and 3) requires to be set up only one time for each nozzle, allowing the reconstruction of patient-specific treatments based on typically-available DICOM data from the treatment plans (images, organ structure contours, and the ion beam plan).

To demonstrate the entire method from start to finish, computational phantoms were used to simulate realistic proton therapy treatments and calculate the incidence cancer risk. To do so, two medulloblastoma-type treatments were simulated based on facility-specific reference measurement data from the Maryland Proton Treatment Center (MPTC). Out-of-field dose was, as expected, shown to be dominated by neutron dose, which was still very low. The organ dose calculations were then used to calculate risk from these treatments. As expected, from a brain treatment and the low scatter dose from neutrons produced within the patient, the resulting risks seem to be low. However, if gamma and neutron measurements are available, it would also be recommended to compare these simulations with treatment facility-specific gamma and neutron measurements, as there may be additional unexpected external dose that needs to be considered.

The currently implied weakness of the Monte Carlo methods is thus its speed, being in general significantly slower than using treatment planning system dose or measurement. Additionally, a considerable amount of time is required to set up accurate proton treatment simulations. However, significant acceleration of dose calculations using Monte Carlo is possible utilizing the NIH Biowulf cluster. Currently, TOPAS has only multithreading capabilities, however, in the future, multiprocessing capabilities will also be available, and this will further speed up simulations. At the moment, this deficiency can be overcome by creating scripts that split the simulations to be run separately and simultaneously on the NIH Biowulf cluster. Because each delivered spot simulation is independent of one another, and the treatments do not have a time-

dependency, the simulations can simply be split into as many separate simulations as there are spots, spot energies, etc. While this will utilize more time on the cluster system, it will be possible to run simulations on the scale of hours instead of days.

4.3.3   Risk calculations

Minimizing the risk from radiotherapy is important for all patients and this is especially the case for young patients. In comparison to older cancer patients, pediatric patients have organs and tissue which are still actively developing. In addition, pediatric patients, ideally, have longer post-treatment lives [63]. Unfortunately, this also means that they have a longer time to develop any secondary effects and a small amount of radiation deposited in a healthy organ or tissue may increase the probability of such an occurrence. Therefore, minimizing the risk of such an occurrence by minimizing the dose delivered to normal tissue needs to be a priority.

In this work, ERR, EAR, and LAR were calculated on two pediatric patient cases recreating the most common pediatric CNS tumor. The risk analysis used risk models recommended by the BEIR VII committee, after communications with NCI epidemiologists to assess the most appropriate method to calculate risk from neutrons due to proton therapy. These models will next be expanded to include the NCI risk models not based on BEIR VII.

Risks could not be estimated for all organs because the unexposed baseline cancer incidence rates for those organs were not measured and data is not available for all organs. In addition, no dose rate factor corrections were used. The BEIR VII risk

models are mostly based on Hiroshima and Nagasaki Life Span Study, a cohort that received an instantaneous dose. For this work, the radiation dose received could also be described as "instantaneous", so further corrections were not done.

While the BEIR VII risk models are currently the most appropriate to use when considering long-term effects, it should be noted that there are several limitations to using these models. To establish the parameters for this model, epidemiologic studies were pooled. However, epidemiological studies are not controlled experiments and thus are subject to bias from unmeasured factors. In addition, the analysis of risk based on organ-specific doses, organ doses received by primary dose were ignored, as these models are not accurate at these dose levels and overestimate the risks [10].

5 CONCLUSION AND FUTURE WORK

5.1 OVERVIEW

In this work, dosimetry methods were established and investigated for use in future epidemiologic studies, and risk models were applied to assess risk of second neoplasms due to active scanning proton therapy treatments. First, methods were used to extend the anatomy available from patient images for studies that require Monte Carlo simulations of out-of-field organ doses. Second, TOPAS Monte Carlo simulation of scatter was benchmarked using the well-validated code, MCNP. Facility-specific measurements were used to create patient-specific treatment dose reconstruction. Modules were also created to pre-process patient DICOM data which was then coupled with facility-specific modules, and input parameters were created. Lastly, post-processing modules combined the voxel-based dose into organ-based doses, and BEIR VII risk models were applied to the two pediatric phantom cases simulated.

5.2   ANATOMY EXTENSION

The author developed a novel method to extend radiological patient images by combining them with available computational phantoms, which was called the Anatomical Predictive Extension (APE) method. It was confirmed that the APE method results in improved dosimetric accuracy for external radiotherapy applications compared to dose calculations based on a reference computational phantom. The APE method will be useful for researchers to more accurately estimate organ doses outside the treatment fields when only partial-body radiological images are available. Finally, as noted before, the discrepancy in anatomy in the border region between phantom and patient anatomies exists in the merged APE phantom. This requires further investigations, for example possible solutions to reduce the discontinuity may involve "smoothing" of defined phantom tissue regions using a process analogous to smoothing of images. This would also require further investigation into how this affects the estimated dose in the out-of-field region.

5.3 BENCHMARKING TOPAS

TOPAS is a relatively new Monte Carlo code, with the establishing publication published by Perl, et al. in 2012 [70]. The code is based on the well-established GEANT4 code, however, the code itself has not been well-established in the areas of neutron scatter and scoring. Simulations were created to compare with measurement and a more well-established code, MCNP. Benchmarking the neutron fluence with MCNP was found to be more appropriate due to detector sensitivity issues for these measurements.

5.4   PROTON MODELING

To model facility-specific proton therapy treatments, methods to reconstruct absorbed dose received during radiation therapy is necessary for epidemiologic studies. Certain methods were investigated to reconstruct patient-specific organ dose from proton therapy treatments based on easily available measurements while keeping the method as general as possible to allow the code to be extended for future dose calculations of patient-specific treatment dose from multiple facilities.

First, simulations and measurements were matched, and in-house modules were created in Python to describe a specific beam delivery system. This allows for the conversion of treatment plans to TOPAS input parameter files by computing the optical and energy properties of every single pencil beam at the nozzle exits, as a function of the nominal beam energy. Then, facility-specific conversion curves are used to convert patient-specific data in the DICOM format using DICOM treatment ion plans to input parameters for TOPAS simulations. The methods presented in this study model the beam optics and energy spectrum of the system and require to be performed just once for each system. The calculated conversion curves established for each facility can then be used for all subsequent treatment plan simulations from that facility.

If simulations are shown to be within commissioning standards, the Monte Carlo simulations will be able to be used clinically. In addition, other studies of clinical interest will also be possible, such as calculating the need to have the treatment planning systems account for linear energy transfer (LET) and relative biological effectiveness (RBE) dose corrections [45].

105

5.5 ORGAN AND RISK CALCULATIONS

Organ dose calculations of these proton therapy treatments allowed for the assessment of risks of the induction of secondary cancer. It has been shown that young patients show significantly higher risks than adults or patients of a large stature. Deep-seated tumors are associated with elevated risks relative to shallow treatment fields [66]. This work showed that, as expected, from active scanning proton therapy, the out-of-field radiation is low. The main contributor to the organ doses are also as expected from neutrons produced within the patient.

In this study, attributable risks for organs outside of the main radiation field for a one-year-old and a five-year-old pediatric phantom receiving active scanning treatments for a medulloblastoma-type tumor were calculated based on the BEIR VII risk model [10]. First, the excess relative risk (ERR) and excess absolute risk (EAR) of cancer induction were calculated in the organs from the time of the treatment up to the age of 100 years. The ERR and EAR value were weighted as recommended by the BEIR VII Committee to calculate the lifetime attributable risk (LAR) for the colon, liver, lung, and bladders of both phantoms.

5.6   FUTURE WORK

Though the risk of leukemia is the most common concern of second cancers, in this study, the risks were not calculated. To calculate radiation-induced leukemia risks, it is necessary to estimate the dose to bone marrow. While developing the methods described in this paper, it was not possible to extract this information directly from the computation phantoms used in this work and therefore requires further investigation into the best methodology of estimating this dose. The computational phantoms used in this work were in the DICOM format. However, they are also available in a binary format with the spongiosa tissue identified. It will be necessary to create a method to first, extract the fluence to the spongiosa layer within the skeletal structures. Then, it is necessary multiply the fluence by the dose response function, which is the function of phantom age, gender, skeletal site, and energy.

REFERENCES

1.   Travis, L.B., et al., *Second Malignant Neoplasms and Cardiovascular Disease Following Radiotherapy.* JNCI Journal of the National Cancer Institute, 2012. **104**(5): p. 357-370.

2.   Smith, M.A., et al., *Outcomes for children and adolescents with cancer: challenges for the twenty-first century.* J Clin Oncol, 2010. **28**(15): p. 2625-34.

3.   O'Dell, M.W. and M.D. Stubblefield, *Cancer rehabilitation principles and practice.* 2009, New York: Demos Medical Pub.

4.   Miller, K.D., et al., *Cancer treatment and survivorship statistics, 2016.* CA Cancer J Clin, 2016. **66**(4): p. 271-89.

5.   Berrington de Gonzalez, A., et al., *Second solid cancers after radiation therapy: a systematic review of the epidemiologic studies of the radiation dose-response relationship.* Int J Radiat Oncol Biol Phys, 2013. **86**(2): p. 224-33.

6.   Raghunathan, D., et al., *Radiation-Induced Cardiovascular Disease.* Curr Atheroscler Rep, 2017. **19**(5): p. 22.

7.   Armstrong, G.T., et al., *Late mortality among 5-year survivors of childhood cancer: a summary from the Childhood Cancer Survivor Study.* J Clin Oncol, 2009. **27**(14): p. 2328-38.

8.   Stovall, M., et al., *Dose reconstruction for therapeutic and diagnostic radiation exposures: use in epidemiological studies.* Radiat Res, 2006. **166**(1 Pt 2): p. 141-57.

9.   Miglioretti, D.L., et al., *Radiation-Induced Breast Cancer Incidence and Mortality from Digital Mammography Screening: A Modeling Study.* Annals of internal medicine, 2016. **164**(4): p. 205-214.

10.   Council, N.R., *Health Risks from Exposure to Low Levels of Ionizing Radiation: BEIR VII Phase 2.* 2006, Washington, DC: The National Academies Press. 422.

11.   Friedman, D.L., et al., *Subsequent neoplasms in 5-year survivors of childhood cancer: the Childhood Cancer Survivor Study.* J Natl Cancer Inst, 2010. **102**(14): p. 1083-95.

12.   Yahalom, J. and C.S. Portlock, *Long-term cardiac and pulmonary complications of cancer therapy.* Heart Fail Clin, 2011. **7**(3): p. 403-11.

13.   Howell, R., *Second Primary Cancers and Cardiovascular Disease after Radiation Therapy. NCRP Report No. 170.* Med Phys, 2012. **39**(12): p. 7729-7731.

14.   White, M.C., et al., *Age and Cancer Risk: A Potentially Modifiable Relationship.* American journal of preventive medicine, 2014. **46**(3 0 1): p. S7-15.

15.   Kamran, S.C., et al., *Therapeutic radiation and the potential risk of second malignancies.* Cancer, 2016. **122**(12): p. 1809-21.

16.   Inskip, P.D., et al., *Radiation-Related New Primary Solid Cancers in the Childhood Cancer Survivor Study: Comparative Radiation Dose Response and Modification of Treatment Effects.* Int J Radiat Oncol Biol Phys, 2016. **94**(4): p. 800-7.

17. Geng, C., et al., *Dose assessment for the fetus considering scattered and secondary radiation from photon and proton therapy when treating a brain tumor of the mother.* Phys Med Biol, 2016. **61**(2): p. 683-95.

18. Schneider, U. and R. Halg, *The Impact of Neutrons in Clinical Proton Therapy.* Front Oncol, 2015. **5**: p. 235.

19. Neuhausen, S.L., *Ethnic differences in cancer risk resulting from genetic variation.* Cancer, 1999. **86**(S11): p. 2575-2582.

20. Kitahara, C.M., et al., *A New Era of Low-Dose Radiation Epidemiology.* Curr Environ Health Rep, 2015. **2**(3): p. 236-49.

21. Okubo, T., *Long-term epidemiological studies of atomic bomb survivors in Hiroshima and Nagasaki: study populations, dosimetry and summary of health effects.* Radiat Prot Dosimetry, 2012. **151**(4): p. 671-3.

22. Preston, D.L., et al., *Studies of mortality of atomic bomb survivors. Report 13: solid cancer and noncancer disease mortality: 1950-1997. 2003.* Radiat Res, 2012. **178**(2): p. Av146-72.

23. United Nations Scientific Committee on the Effects of Atomic Radiation, U., *Sources and effects of ionizing radiation : UNSCEAR 2000 report to the General Assembly, with scientific annexes Vol. 2, Vol. 2.* 2000, New York: United Nations.

24. Tables, N.-C.W.G.t.R.t.N.R., et al., *Report of the NCI-CDC Working Group to revise the 1985 NIH Radioepidemiological Tables.* 2003, [Bethesda, MD]: U.S.

Dept. of Health and Human Services, National Institutes of Health, National Cancer Institute.

25. Kocher, D.C., A.I. Apostoaei, and F.O. Hoffman, *Radiation effectiveness factors for use in calculating probability of causation of radiogenic cancers.* Health Phys, 2005. **89**(1): p. 3-32.

26. Little, M.P., *Comparison of the risks of cancer incidence and mortality following radiation therapy for benign and malignant disease with the cancer risks observed in the Japanese A-bomb survivors.* Int J Radiat Biol, 2001. **77**(4): p. 431-64.

27. Kukush, A., et al., *Methods for estimation of radiation risk in epidemiological studies accounting for classical and Berkson errors in doses.* Int J Biostat, 2011. **7**(1): p. 15.

28. Glide-Hurst, C.K. and I.J. Chetty, *Improving radiotherapy planning, delivery accuracy, and normal tissue sparing using cutting edge technologies.* J Thorac Dis, 2014. **6**(4): p. 303-18.

29. Bekelman, J.E., et al., *Principles and reality of proton therapy treatment allocation.* Int J Radiat Oncol Biol Phys, 2014. **89**(3): p. 499-508.

30. Merchant, T.E., et al., *Proton versus photon radiotherapy for common pediatric brain tumors: comparison of models of dose characteristics and their relationship to cognitive function.* Pediatr Blood Cancer, 2008. **51**(1): p. 110-7.

31.   Mzenda, B., et al., *Modeling and dosimetric performance evaluation of the RayStation treatment planning system.* J Appl Clin Med Phys, 2014. **15**(5): p. 4787.

32.   Bednarz, B., J. Daartz, and H. Paganetti, *Dosimetric accuracy of planning and delivering small proton therapy fields.* Phys Med Biol, 2010. **55**(24): p. 7425-38.

33.   Newhauser, W.D., et al., *A Review of Radiotherapy-Induced Late Effects Research after Advanced Technology Treatments.* Front Oncol, 2016. **6**: p. 13.

34.   Huang, J.Y., et al., *Accuracy and sources of error of out-of field dose calculations by a commercial treatment planning system for intensity-modulated radiation therapy treatments.* J Appl Clin Med Phys, 2013. **14**(2): p. 4139.

35.   Howell, R.M., et al., *Accuracy of out-of-field dose calculations by a commercial treatment planning system.* Phys Med Biol, 2010. **55**(23): p. 6999-7008.

36.   Wang, L. and G.X. Ding, *The accuracy of the out-of-field dose calculations using a model based algorithm in a commercial treatment planning system.* Phys Med Biol, 2014. **59**(13): p. N113-28.

37.   Schneider, U., et al., *Accuracy of out-of-field dose calculation of tomotherapy and cyberknife treatment planning systems: a dosimetric study.* Z Med Phys, 2014. **24**(3): p. 211-5.

38.   Lee, C., et al., *Reconstruction of organ dose for external radiotherapy patients in retrospective epidemiologic studies.* Phys Med Biol, 2015. **60**(6): p. 2309-24.

39.   Joosten, A., et al., *Evaluation of organ-specific peripheral doses after 2-dimensional, 3-dimensional and hybrid intensity modulated radiation therapy for*

breast cancer based on Monte Carlo and convolution/superposition algorithms: implications for secondary cancer risk assessment. Radiother Oncol, 2013. **106**(1): p. 33-41.

40.   Murray, L.J., et al., *Radiation-induced second primary cancer risks from modern external beam radiotherapy for early prostate cancer: impact of stereotactic ablative radiotherapy (SABR), volumetric modulated arc therapy (VMAT) and flattening filter free (FFF) radiotherapy.* Physics In Medicine And Biology, 2015. **60**(3): p. 1237-1257.

41.   Lomax, A.J., et al., *A treatment planning inter-comparison of proton and intensity modulated photon radiotherapy.* Radiother Oncol, 1999. **51**(3): p. 257-71.

42.   Athar, B.S. and H. Paganetti, *Neutron equivalent doses and associated lifetime cancer incidence risks for head & neck and spinal proton therapy.* Phys Med Biol, 2009. **54**(16): p. 4907-26.

43.   Hall, E.J., *Intensity-modulated radiation therapy, protons, and the risk of second cancers.* Int J Radiat Oncol Biol Phys, 2006. **65**(1): p. 1-7.

44.   Mohan, R. and D. Grosshans, *Proton therapy - Present and future.* Adv Drug Deliv Rev, 2017. **109**: p. 26-44.

45.   Paganetti, H., *Relative biological effectiveness (RBE) values for proton beam therapy. Variations as a function of biological endpoint, dose, and linear energy transfer.* Phys Med Biol, 2014. **59**(22): p. R419-72.

46.   Therapy, T.N.A.f.P. *Proton Therapy Centers In Operation*. 2016 [cited 2017 November 4th]; Available from: http://www.proton-therapy.org/map.htm.

47.   Danial, S., S. Dariush, and M.S. Jozani, *Characteristics of a heavy water photoneutron source in boron neutron capture therapy.* Chinese Physics C, 2013. **37**(7): p. 078201.

48.   Birgani, M.T., et al., *Breast Radiotherapy with Mixed Energy Photons; a Model for Optimal Beam Weighting.* Asian Pac J Cancer Prev, 2015. **16**(17): p. 7785-8.

49.   Janiszewska, M., et al., *Secondary radiation dose during high-energy total body irradiation.* Strahlenther Onkol, 2014. **190**(5): p. 459-66.

50.   Yabuta, K., et al., *[Neutron Dosimetry System Using CR-39 for High-energy X-ray Radiation Therapy].* Igaku Butsuri, 2014. **34**(3): p. 139-48.

51.   Zacharatou Jarlskog, C., et al., *Assessment of organ-specific neutron equivalent doses in proton therapy using computational whole-body age-dependent voxel phantoms.* Physics In Medicine And Biology, 2008. **53**(3): p. 693-717.

52.   Vykydal, Z., et al., *Measurement of Secondary Neutrons Generated during Proton Therapy.* Radiat Prot Dosimetry, 2016. **172**(4): p. 341-345.

53.   Howell, R.M., et al., *Measured Neutron Spectra and Dose Equivalents From a Mevion Single-Room, Passively Scattered Proton System Used for Craniospinal Irradiation.* Int J Radiat Oncol Biol Phys, 2016. **95**(1): p. 249-57.

54.   Halg, R.A., et al., *Measurements of the neutron dose equivalent for various radiation qualities, treatment machines and delivery techniques in radiation therapy.* Phys Med Biol, 2014. **59**(10): p. 2457-68.

55.   Zacharatou Jarlskog, C. and H. Paganetti, *Risk of developing second cancer from neutron dose in proton therapy as function of field characteristics, organ, and patient age.* Int J Radiat Oncol Biol Phys, 2008. **72**(1): p. 228-35.

56.   Kry, S.F., et al., *AAPM TG 158: Measurement and calculation of doses outside the treated volume from external-beam radiation therapy.* Med Phys, 2017. **44**(10): p. e391-e429.

57.   Wroe, A., et al., *Out-of-field dose equivalents delivered by passively scattered therapeutic proton beams for clinically relevant field configurations.* Int J Radiat Oncol Biol Phys, 2009. **73**(1): p. 306-13.

58.   Soppera, N., M. Bossant, and E. Dupont, *JANIS 4: An Improved Version of the NEA Java-based Nuclear Data Information System.* Nuclear Data Sheets, 2014. **120**: p. 294-296.

59.   Jiang, H., et al., *Simulation of organ-specific patient effective dose due to secondary neutrons in proton radiation treatment.* Physics In Medicine And Biology, 2005. **50**(18): p. 4337-4353.

60.   Howell, R.M. and E.A. Burgett, *Secondary neutron spectrum from 250-MeV passively scattered proton therapy: measurement with an extended-range Bonner sphere system.* Med Phys, 2014. **41**(9): p. 092104.

61.   Perez-Andujar, A., R. Zhang, and W. Newhauser, *Monte Carlo and analytical model predictions of leakage neutron exposures from passively scattered proton therapy.* Med Phys, 2013. **40**(12): p. 121714.

62.	Perez-Andujar, A., W.D. Newhauser, and P.M. Deluca, *Neutron production from beam-modifying devices in a modern double scattering proton therapy beam delivery system.* Phys Med Biol, 2009. **54**(4): p. 993-1008.

63.	Matsumoto, S., et al., *Secondary Neutron Doses to Pediatric Patients During Intracranial Proton Therapy: Monte Carlo Simulation of the Neutron Energy Spectrum and its Organ Doses.* Health Phys, 2016. **110**(4): p. 380-6.

64.	Stichelbaut, F., M. Closset, and Y. Jongen, *Secondary neutron doses in a compact proton therapy system.* Radiat Prot Dosimetry, 2014. **161**(1-4): p. 368-72.

65.	Athar, B.S., et al., *Comparison of out-of-field photon doses in 6 MV IMRT and neutron doses in proton therapy for adult and pediatric patients.* Phys Med Biol, 2010. **55**(10): p. 2879-91.

66.	Athar, B.S. and H. Paganetti, *Comparison of second cancer risk due to out-of-field doses from 6-MV IMRT and proton therapy based on 6 pediatric patient treatment plans.* Radiother Oncol, 2011. **98**(1): p. 87-92.

67.	Newhauser, W.D., et al., *The risk of developing a second cancer after receiving craniospinal proton irradiation.* Physics In Medicine And Biology, 2009. **54**(8): p. 2277-2291.

68.	Bauer, J., et al., *Integration and evaluation of automated Monte Carlo simulations in the clinical practice of scanned proton and carbon ion beam therapy.* Phys Med Biol, 2014. **59**(16): p. 4635-59.

116

69.   Geyer, A.M., et al., *The UF/NCI family of hybrid computational phantoms representing the current US population of male and female children, adolescents, and adults--application to CT dosimetry.* Phys Med Biol, 2014. **59**(18): p. 5225-42.

70.   Perl, J., et al., *TOPAS: an innovative proton Monte Carlo platform for research and clinical applications.* Med Phys, 2012. **39**(11): p. 6818-37.

71.   Diallo, I., et al., *Estimation of the radiation dose delivered to any point outside the target volume per patient treated with external beam radiotherapy.* Radiother Oncol, 1996. **38**(3): p. 269-71.

72.   Jagetic, L.J. and W.D. Newhauser, *A simple and fast physics-based analytical method to calculate therapeutic and stray doses from external beam, megavoltage x-ray therapy.* Phys Med Biol, 2015. **60**(12): p. 4753-75.

73.   Taddei, P.J., et al., *Analytical model for out-of-field dose in photon craniospinal irradiation.* Phys Med Biol, 2013. **58**(21): p. 7463-79.

74.   Xu, X.G., B. Bednarz, and H. Paganetti, *A review of dosimetry studies on external-beam radiation treatment with respect to second cancer induction.* Physics In Medicine And Biology, 2008. **53**(13): p. R193-241.

75.   Diallo, I., et al., *Frequency distribution of second solid cancer locations in relation to the irradiated volume among 115 patients treated for childhood cancer.* Int J Radiat Oncol Biol Phys, 2009. **74**(3): p. 876-83.

76.   Xu, X.G., *An exponential growth of computational phantom research in radiation protection, imaging, and radiotherapy: a review of the fifty-year history.* Phys Med Biol, 2014. **59**(18): p. R233-302.

77.   Petoussi-Henss, N., M. Zankl, and D. Nosske, *Estimation of patient dose from radiopharmaceuticals using voxel models.* Cancer Biother Radiopharm, 2005. **20**(1): p. 103-9.

78.   Lee, C., et al., *The UF family of reference hybrid phantoms for computational radiation dosimetry.* Phys Med Biol, 2010. **55**(2): p. 339-63.

79.   Fippel, M., *Fast Monte Carlo dose calculation for photon beams based on the VMC electron algorithm.* Med Phys, 1999. **26**(8): p. 1466-75.

80.   Chetty, I.J., et al., *Report of the AAPM Task Group No. 105: Issues associated with clinical implementation of Monte Carlo-based photon and electron external beam treatment planning.* Med Phys, 2007. **34**(12): p. 4818-53.

81.   Paganetti, H., *Range uncertainties in proton therapy and the role of Monte Carlo simulations.* Phys Med Biol, 2012. **57**(11): p. R99-117.

82.   Perl, J., et al., *TOPAS: An innovative proton Monte Carlo platform for research and clinical applications.* Med Phys, 2012. **39**(11): p. 6818-37.

83.   Hu, Z.M., et al., *Monte Carlo simulation of a Bonner sphere spectrometer for application to the determination of neutron field in the Experimental Advanced Superconducting Tokamak experimental hall.* Rev Sci Instrum, 2014. **85**(11): p. 11e417.

84. Enger, S.A., et al., *Monte Carlo calculations of thermal neutron capture in gadolinium: a comparison of GEANT4 and MCNP with measurements.* Med Phys, 2006. **33**(2): p. 337-41.

85. Pshenichnov, I., I. Mishustin, and W. Greiner, *Neutrons from fragmentation of light nuclei in tissue-like media: a study with the GEANT4 toolkit.* Phys Med Biol, 2005. **50**(23): p. 5493-507.

86. Bohlen, T.T., et al., *Benchmarking nuclear models of FLUKA and GEANT4 for carbon ion therapy.* Phys Med Biol, 2010. **55**(19): p. 5833-47.

87. Sawkey, D., M. Constantin, and M. Svatos, *Comparison of electron scattering algorithms in Geant4.* Phys Med Biol, 2012. **57**(11): p. 3249-58.

88. Faddegon, B.A., et al., *Experimental depth dose curves of a 67.5 MeV proton beam for benchmarking and validation of Monte Carlo simulation.* Med Phys, 2015. **42**(7): p. 4199-210.

89. Jarlskog, C.Z. and H. Paganetti, *Physics Settings for Using the Geant4 Toolkit in Proton Therapy.* IEEE Transactions on Nuclear Science, 2008. **55**(3): p. 1018-1025.

90. Jia, S.B., et al., *Evaluation of energy deposition and secondary particle production in proton therapy of brain using a slab head phantom.* Rep Pract Oncol Radiother, 2014. **19**(6): p. 376-84.

91. Jones, B., et al., *Fast neutron relative biological effects and implications for charged particle therapy.* Br J Radiol, 2011. **84 Spec No 1**: p. S11-8.

92.   Tiyapun, K., et al., *Validation of the MCNP computational model for neutron flux distribution with the neutron activation analysis measurement.* Journal of Physics: Conference Series, 2015. **611**(1): p. 012007.

93.   Lewis, B.J., et al., *Review of bubble detector response characteristics and results from space.* Radiat Prot Dosimetry, 2012. **150**(1): p. 1-21.

94.   Kry, S.F., et al., *Neutron spectra and dose equivalents calculated in tissue for high-energy radiation therapy.* Med Phys, 2009. **36**(4): p. 1244-50.

95.   Conlin, J.L., et al., *Listing of Available ACE Data Tables.* 2014, ; Los Alamos National Lab. (LANL), Los Alamos, NM (United States). p. Medium: ED.

96.   Chadwick, M.B., et al., *ENDF/B-VII.1 Nuclear Data for Science and Technology: Cross Sections, Covariances, Fission Product Yields and Decay Data.* Nuclear Data Sheets, 2011. **112**(12): p. 2887-2996.

97.   Sawakuchi, G.O., et al., *An MCNPX Monte Carlo model of a discrete spot scanning proton beam therapy nozzle.* Med Phys, 2010. **37**(9): p. 4960-70.

98.   Grevillot, L., et al., *A Monte Carlo pencil beam scanning model for proton treatment plan simulation using GATE/GEANT4.* Phys Med Biol, 2011. **56**(16): p. 5203-19.

99.   Grassberger, C., A. Lomax, and H. Paganetti, *Characterizing a proton beam scanning system for Monte Carlo dose calculation in patients.* Phys Med Biol, 2015. **60**(2): p. 633-45.

100. Lorin, S., et al., *Reference dosimetry in a scanned pulsed proton beam using ionisation chambers and a Faraday cup.* Phys Med Biol, 2008. **53**(13): p. 3519-29.

101. Medin, J., *Implementation of water calorimetry in a 180 MeV scanned pulsed proton beam including an experimental determination of kQ for a Farmer chamber.* Phys Med Biol, 2010. **55**(12): p. 3287-98.

102. Clasie, B., et al., *Golden beam data for proton pencil-beam scanning.* Phys Med Biol, 2012. **57**(5): p. 1147-58.

103. Lomax, A.J., et al., *Treatment planning and verification of proton therapy using spot scanning: initial experiences.* Med Phys, 2004. **31**(11): p. 3150-7.

104. Goma, C., et al., *Proton beam monitor chamber calibration.* Phys Med Biol, 2014. **59**(17): p. 4961-71.

105. ICRP, *Relative biological effectiveness (RBE), quality factor (Q), and radiation weighting factor (w(R)). A report of the International Commission on Radiological Protection.* Ann ICRP, 2003. **33**(4): p. 1-117.

106. Zhang, R., et al., *Comparison of risk of radiogenic second cancer following photon and proton craniospinal irradiation for a pediatric medulloblastoma patient.* Phys Med Biol, 2013. **58**(4): p. 807-23.

107. Zacharatou Jarlskog, C., et al., *Assessment of organ-specific neutron equivalent doses in proton therapy using computational whole-body age-dependent voxel phantoms.* Phys Med Biol, 2008. **53**(3): p. 693-717.

108.   Preston, D.L., et al., *Studies of mortality of atomic bomb survivors. Report 13: Solid cancer and noncancer disease mortality: 1950-1997.* Radiation research, 2003. **160**(4): p. 381-407.

109.   Ródenas, J., A. Martinavarro, and V. Rius, *Validation of the MCNP code for the simulation of Ge-detector calibration.* Nuclear Instruments and Methods in Physics Research Section A: Accelerators, Spectrometers, Detectors and Associated Equipment, 2000. **450**(1): p. 88-97.

110.   Donzella, A., et al., *Experimental validation of MCNP simulations for the EURITRACK Tagged Neutron Inspection System.* Nuclear Instruments and Methods in Physics Research Section B: Beam Interactions with Materials and Atoms, 2007. **261**(1): p. 291-294.

111.   Mashnik, S.G., *Validation and verification of MCNP6 against intermediate and high-energy experimental data and results by other codes.* The European Physical Journal Plus, 2011. **126**(5): p. 49.

112.   Zheng, Z., Q. Mei, and H. Li, *Validation and Application of MCNP and TORT Source Generation Codes.* Energy Procedia, 2017. **127**: p. 255-263.

113.   Nedaie, H.A., et al., *Neutron dose measurements of Varian and Elekta linacs by TLD600 and TLD700 dosimeters and comparison with MCNP calculations.* J Med Phys, 2014. **39**(1): p. 10-7.

114.   Kry, S.F., et al., *AAPM TG 158: Measurement and calculation of doses outside the treated volume from external-beam radiation therapy.* Medical Physics, 2017. **44**(10): p. e391-e429.

115.   Zhang, R., et al., *An analytic model of neutron ambient dose equivalent and equivalent dose for proton radiotherapy.* Phys Med Biol, 2010. **55**(23): p. 6975-85.

116.   Anferov, V., *Analytic estimates of secondary neutron dose in proton therapy.* Phys Med Biol, 2010. **55**(24): p. 7509-22.

117.   Zhu, J. and S.N. Penfold, *Dosimetric comparison of stopping power calibration with dual-energy CT and single-energy CT in proton therapy treatment planning.* Med Phys, 2016. **43**(6): p. 2845-2854.

118.   Schneider, U., E. Pedroni, and A. Lomax, *The calibration of CT Hounsfield units for radiotherapy treatment planning.* Phys Med Biol, 1996. **41**(1): p. 111-24.